Kinematic and geochronological constraints on shear deformation in the Ferriere-Mollières shear zone (Argentera-Mercantour Massif, Western Alps): implications for the evolution of the Southern

DOI:10.1007/s00531-018-1593-y

Kinematic and geochronological constraints on shear deformation in the Ferriere-Mollières shear zone (Argentera-Mercantour Massif, Western Alps): implications for the evolution of the Southern European Variscan Belt

Complete List of Authors:

Simonetti, Matteo*;
Università degli Studi di Torino, Dipartimento di Scienze della Terra, via V. Caluso 35,10125 Torino, matteo.simonetti@unito.it
ORCID ID: 0000-0002-8843-7615

Carosi, Rodolfo;
Università degli Studi di Torino, Dipartimento di Scienze della Terra, via V. Caluso 35,10125 Torino, tel. +39 0116705864, rodolfo.carosi@unito.it
ORCID ID: 0000-0002-6561-7090

Montomoli, Chiara;
Università degli Studi di Pisa, Dipartimento di Scienze della Terra, via S. Maria 53,56126 Pisa, tel. +390502215758, chiara.montomoli@unipi.it
IGG-CNR PISA, via Moruzzi 1, Pisa, Italy
ORCID ID: 0000-0002-0364-5395

Langone, Antonio;
IGG-CNR U.O.S. of Pavia, Via Ferrata 1, Pavia, Italy; langone@crystal.unipv.it
ORCID ID: 0000-0002-7346-2922

D'Addario, Enrico;
Università degli Studi di Pisa, Dipartimento di Scienze della Terra, via S. Maria 53,56126 Pisa; endadda@gmail.com

Mammoliti, Elisa;
Università degli Studi di Pisa, Dipartimento di Scienze della Terra, via S. Maria 53,56126 Pisa; elisamammoliti@ymail.com

* Corresponding author matteo.simonetti@unito.it

Kinematic and geochronological constraints on shear deformation in the Ferriere-Mollières shear zone (Argentera-Mercantour Massif, Western Alps): implications for the evolution of the Southern European Variscan Belt

Simonetti M.[a*], Carosi R.[a,] , Montomoli C. [b, c], Langone A.[d], D'Addario E.[b], Mammoliti E.[b]

a) *Dipartimento di Scienze della Terra, Universita` di Torino, Via Valperga Caluso, 35, Torino, Italy;*

b) *Dipartimento di Scienze della Terra, Universita` di Pisa, Via S. Maria, 53, Pisa, Italy;*

c) IGG-CNR PISA, via Moruzzi 1, Pisa, Italy;

d) *IGG-CNR U.O.S. of Pavia, Via Ferrata 1, Pavia, Italy;*

* Corresponding author Email: matteo.simonetti@unito.it

Abstract

In the Western Alps a steeply dipping km-scale shear zone (the Ferriere-Mollières shear zone) cross-cuts Variscan migmatites in the Argentera-Mercantour External Crystalline Massif.

Structural analysis joined with kinematic vorticity and finite strain analyses allowed to recognize a high-temperature deformation associated to dextral transpression characterized by a variation in the percentage of pure shear and simple shear along a deformation gradient. U-Th-Pb dating of syn-kinematic monazites was performed on mylonites. The oldest ~340 Ma ages were obtained in protomylonites whereas ages of ~ 320 Ma were found in mylonites from the core of the shear zone. These ages indicate that the Ferriere-Mollières shear zone is a still preserved Variscan shear zone.

Ages of ~320 Ma obtained in this work are in agreement with ages of the dextral transpressional shear zones occurring in the Maures-Tanneron Massif and Corsica-Sardinia. However, transpression in the Argentera-Mercantour Massif started earlier than in other sectors of the southern Variscan Belt. This is possibly caused by the curvature of the belt triggering the progressive migration of shear deformation. Our data allow a correlation between the Argentera-Mercantour Massif and other segments of the Southern European Variscan Belt, in particular with Maures-Tanneron Massif and Corsica-Sardinia and contribute to fill a gap in the age of activity and in the kinematics of the flow of the system of dextral shear zones of the southern portion of the EVSZ.

Key words: Transpression, Argentera-Mercantour Massif, Mylonites, East Variscan Shear Zone, Monazite

1. Introduction

The European Variscan Belt is the result of a Devonian–Carboniferous continent-continent collision (Arthaud and Matte, 1977; Burg and Matte, 1978; Tollmann, 1982; Matte, 1986a,b; Franke, 1989) between Laurentia-Baltica and Gondwana (Matte, 1986a, 2001). Between these two continents, small microplates existed, defined essentially on the basis of palaeomagnetism and palaeobiostratigraphy (Scotese and McKerrow, 1990; Franke et al., 2017, with references therein). The main microplates are known as Avalonia and Armorica (Matte, 2001). They broke away from Gondwana during the early Palaeozoic, prior to docking against Baltica and Laurentia before the Devonian-Carboniferous collision (Matte, 2001).

The Architecture of the Variscan Belt is well defined in eastern, central and western Europe (Matte, 1986b, 2001; Fluck et al., 1991; Ballévre et al., 2009; Faure et al. 2009; Skrzypek et al., 2012) where the Saxothuringian Zone (southwestern Iberian Massif, northern Armorican Massif, Vosges and Bohemian Massif) and the Moldanubian Zone (southern Iberian Massif, central and southern Vosges, Massif Central, southern Armorican Massif and southern Bohemian Massif) are recognized (Fig. 1a).

In contrast, the structural arrangement of the SE segment of the European Variscan Belt is less clear because of tectonic reworking during Alpine Orogeny.

Some authors proposed that the European Variscan Belt is characterized by a composite orocline, developed because of indentation tectonics (Matte and Ribeiro, 1975; Matte, 1986a,b), made by two main branches: the well-known western Ibero–Armorican arc (Matte and Ribeiro, 1975; Brun and Burg, 1982; Dias and Ribeiro, 1995; Dias et al., 2016; Fernández-Lozano et al., 2016) and the eastern branch (Matte, 2001; Bellot, 2005), delimited by a system of regional-scale dextral, transpressive shear zones known as the East Variscan Shear Zone (EVSZ; Corsini and Rolland, 2009; Carosi et al., 2012; Padovano et al., 2012, 2014). The EVSZ is actually less understood, expecially in the sectors that are now part of the Alps.

Although during the Carboniferous extensive transpressive shear deformation is recognized in several fragments belonging to the Southern European Variscan Belt (Matte, 1986a,b; Carosi and Palmeri, 2002; Iacopini et al., 2008; Frassi et al., 2009; Carosi et al., 2012; Corsini and Rolland, 2009; Guillot et al., 2009; Schneider et al., 2014), the impact of this deformation on the arrangement of the belt needs further constraints.

A deeper knowledge of Variscan deformation is of great importance for enhancing correlations between the fragments of the belt in the Mediterranean area since these correlations are mostly based on lithological and stratigraphic affinities and paleomagnetic data. In particular, the correlation between Corsica-Sardinia Block, Maures-Tanneron Massif and Variscan basement of the Western Alps (External Crystalline Massifs) is still debated. According to some authors these three sectors should have been in continuity during Variscan orogenesis (Rollet et al., 2002; Rosenbaum et al., 2002;

Advokaat et al., 2014), while according to Stampfli et al. (2002), Turco et al. (2012), von Raumer et al. (2013), the Corsica-Sardinia Block was located in a more westerly position connected to Iberia and therefore, away from southern France and the future Alpine External Crystalline Massifs.

In the Western Alps, the Variscan External Crystalline Massifs are cross-cut by km-scale shear zones whose age of activity and deformation regime are not entirely clear. It is also not clear whether these shear zones have been fully reactivated during the Alpine orogeny, or if evidence of Variscan deformation is still preserved.

A useful method to date shear zone activity, especially when developed under high-temperature conditions, is the U-Th-Pb geochronology on syn-kinematic monazite (Williams et al., 2007). Reliable results were obtained in the Himalayan belt in dating both the activity of regional–scale shear zones (Carosi et al., 2010; Montomoli et al., 2013, 2015; Cottle et al., 2015; Iaccarino et al., 2015, 2017; Carosi et al., 2016a) and metamorphic events (Khon et al., 2005; Khon, 2008; Larson and Cottle, 2015). In high-temperature shear zones, this method is more reliable than the $^{40}Ar/^{39}Ar$ method because argon isotopes are often mobile during deformation (Dunlap et al., 1991; Mulch and Cosca, 2004; Villa et al., 1997, 2014; Villa, 2015; Challandes et al., 2003, 2008; Sanchez et al., 2011).

In the present work we focus on the northern sector of the Ferriere-Mollières shear zone (FMSZ; Faure-Muret, 1955; Malaroda et al., 1970; Compagnoni et al., 2010) located in the Argentera-Mercantour Massif, a km-scale shear zone in the Alpine External Crystalline Massifs. The FMSZ is constituted by mylonites developed from Variscan migmatites and leucogranites (Musumeci and Colombo, 2002; Carosi et al., 2016b). Conflicting deformation ages have been proposed: Musumeci and Colombo (2002) obtained a cooling age for mylonitic leucogranite of 327 ± 3 Ma (whole rock Rb/Sr ages on magmatic muscovite grains) interpreted as the younger limit of the FMSZ activity. Corsini et al. (2004) and Sanchez et al. (2011) proposed deformation ages of ~ 22 and ~ 20 Ma ($^{40}Ar/^{39}Ar$ on phengites from mylonitic micaschists and from ultramylonites of the Argentera granite), suggesting a reactivation of the Variscan shear zone (e.g. Valetta shear zone) and formation of new shear zones (e.g Fremamorta-Colle del Sabbione shear zone) during Alpine orogeny under greenschist metamorphic conditions.

This paper aims to clarify both the kinematics of the flow and the age of activity of the FMSZ in order to check if Variscan deformation structures are still preserved and if dextral shear deformation affecting the Alpine External Crystalline Massifs can be linked to the activity of other similar transpressional shear zones in the Southern European Variscan Belt. To verify this hypothesis, we carried out a kinematic vorticity analysis and a U-Th-Pb geochronological study on syn-kinematic monazites, combined with structural and microstructural analyses on different types of mylonites recently mapped by Carosi et al. (2016b).

2. Geological Setting of the Argentera-Mercantour Massif

The External Crystalline Massifs in the Western Alps are, together with the Corsica-Sardinia Block and the Maures-Tanneron Massif, fragments of the Variscan Belt well-preserved within the Mediterranean area.

The Argentera-Mercantour Massif is constituted by the Gesso-Stura-Vésubie (GSV) and the Tinée (TMC) metamorphic complexes (Malaroda et al., 1970; Compagnoni et al., 2010) which are separated by the FMSZ (Fig. 1b). The GSV complex is made of migmatitic gneiss derived from Late Ordovician granitoids and migmatitic paragneiss. Ferrando et al. (2008) and Compagnoni et al. (2010) recognized a metamorphic evolution characterized by: 1) HP metamorphic peak; 2) initial decompression stage; 3) HT–MP amphibolite-facies metamorphism; 4) LT–LP amphibolite-facies metamorphism.

The TMC migmatites resulted from partial melting of metasediments. Eclogite relicts are reported by Faure-Muret (1955) and Malaroda et al. (1970). According to Compagnoni et al. (2010) the TMC shows a minor degree of melting than the migmatites of the GSV complex as testified by a smaller proportion of leucosomes. A greenschist facies imprint is mainly due to a system of ductile to brittle-ductile shear zones (Baietto et al., 2009) affecting the whole Argentera-Mercantour Massif (Corsini et al., 2004; Sanchez et al., 2011). The main Alpine faults of the Argentera-Mercantour Massif are the NW-SE Bersezio Fault Zone, in the central part, and the E-W Fremamorta-Colle Sabbione Shear Zone, in the southernmost part of the massif (Fig. 1b).

The FMSZ (also known as Valletta shear zone; Corsini et al., 2004) strikes NW–SE and extends for about 20 km (Fig. 1b) with a thickness between 100 m to the south-east and more than 1000 m to the north-west. The fault rocks in the FMSZ resulted from the shearing of migmatites of the GSV and the TMC. The transition from non-sheared migmatites to protomylonites, mylonites and ultramylonites can be observed along a deformation gradient towards the center of the shear zone (Fig. 2; Carosi et al., 2016b). The rocks in the shear zone are medium-grained dark mylonitic schists with biotite and white mica ± garnet. Mylonites and ultramylonites with chlorite and white mica also occur in the central part of the shear zone while mylonites and protomylonites with biotite and sillimanite ± garnet are present in the margins of the shear zone. Because of the constant orientation of the mylonitic foliation, the mineral lineation and the sense of shear in all the rocks inside the FMSZ, Carosi et al. (2016b) interpreted these parageneses as linked to an evolution of the deformation under decreasing temperature.

3. Structural Analysis

3.1 Variscan shear zone

The main structural elements in the FMSZ are a mylonitic foliation defined by the preferred orientation of biotite + white mica and a protomylonitic foliation with biotite + sillimanite in the external part of the shear zone, both striking N100-140 and steeply dipping towards the northeast or the southwest (Fig. 2). A mineral lineation, defined by a preferred alignement of stretched quartz and feldspar, trends N110-130 and dips 20° towards the northwest (Fig. 2).

In protomylonites the foliation is an anastomosed disjunctive cleavage (Passchier and Trouw, 2005) formed by alternating coarse-grained layers of deformed quartz and feldspar and biotite- and sillimanite-rich layers (Fig. 3a,b). Sillimanite occurs both in prismatic and fibrolitic habitus. In the mylonites, a transition can be observed from a disjunctive cleavage with sub-parallel cleavage domains, formed by alternating layers of deformed quartz and biotite + white mica (Fig. 3c,d), to a continuous cleavage in the most intensely deformed ultramylonites rich in phyllosilicates (Fig. 3e,f). The mylonitic foliation underwent a later gentle folding of uncertain age with axial planes moderately dipping toward the SW and NW-SE trending axes (Fig. 2). Kinematic indicators (S-C' fabric, micafish, mantled porphyroclasts and quartz oblique foliation) indicate a strike-slip component of movement with a minor reverse, top-to-the-SE, component where the foliation dips northeast (Fig. 4a,b,c) and with a minor normal component where it dips southwest. Quartz shows subgrain rotation recrystallization (Piazolo and Passchier, 2002; Stipp et al., 2002) and only very minor effects of grain boundary migration in mylonites (Fig. 4d) and ultramylonites. Quartz in protomylonites is mainly affected by grain boundary migration (Piazolo and Passchier, 2002; Stipp et al., 2002). Feldspar shows undulose extinction due to ductile deformation (Fig. 4e) and does not show evidence of brittle deformation. The thickness of the FMSZ progressively decreases from NW to SE. The maximum thickness of ~2 km is reached to the NW, in the Ferriere village area (Fig. 1b). Thickness variations of the different types of mylonites, at a local scale, were also reported (in agreement with Carosi et al., 2016b, Fig. 2). In the wall rocks of the FMSZ, in the GSV and TMC complex, Carosi et al. (2016b) and Simonetti et al. (2017) recognized outcrop-scale open to tight symmetric upright folds with NW-SE oriented axial plane and NW dipping axis deforming the main foliation of the migmatites.

3.2 Alpine Shear Zones

Shear zones cross-cutting the mylonites of the FMSZ (Fig. 2) and the migmatites of the two metamorphic complexes have been identified (Fig. 5a). These shear zones have metric to decametric thickness with lateral continuities up to several hundred meters. They consist of fine-grained mylonites or phyllonites with quartz and feldspar porphyroclasts in a fine-grained chlorite + white mica matrix. This paragenesis is indicative of greenschist facies metamorphism. Biotite relicts, indicating an older, higher temperature foliation, are still recognizable. The proportion of matrix is ~ 65% -

75%. The foliation strikes nearly E-W and dips at moderate to low angles toward the north with a north plunging mineral lineation.

The foliation is a spaced cleavage defined by the preferred orientation of chlorite and white mica. Kinematic indicators, mainly micafish and S-C and S-C' fabrics, indicate a top-to-the-S reverse sense of shear (Fig. 5b). C and C' planes are characterized by the presence of fine-grained chlorite. Along the S foliation biotite relicts are sometimes present (Fig. 5c). Quartz shows undulose extinction and subgrains, the latter indicating subgrain rotation recrystallization (Piazolo and Passchier, 2002; Stipp et al., 2002) as the dominant deformation mechanism. Feldspar shows undulose extinction and deformation lamellae while some fractured porphyroclasts are also present.

4. Kinematics and vorticity of the flow of the FMSZ

Deformation in shear zones is often approximate to simple shear, especially in high-strain zones (Passchier 1987, 1991; Iacopini et al., 2010, 2011). However, a significative component of pure shear has been detected in many regional-scale shear zones around the world, under various metamorphic conditions (Carosi and Palmeri, 2002, Carosi et al., 2005; Carosi et al., 2006, 2007; Festa et al., 2016; Goscombe et al., 2003, 2005; Iacopini et al., 2008; Kurz and Northrup, 2008; Larson and Godin, 2009; Law et al., 2004; Li et al., 2016; Nabavi et al., 2016; Sarkarinejad and Azizi, 2008; Sarkarinejad et al., 2015; Wu et al., 2016; Xypolias and Kokkalas, 2006; Zang and Teyssier, 2013).

In order to characterize the type of flow and the deformation of the FMSZ, a kinematic vorticity analysis was performed on mylonites collected along three transects (A, B and C) perpendicular to the shear zone boundaries and parallel to the deformation gradient (Fig. 6). In addition, we performed a finite strain analysis in order to obtain the axial ratio of the finite strain ellipsoid (Rxz),which is indispensable for calculating the shortening perpendicular to the flow plane.

4.1 Methods

Pure and simple shear can be expressed through the dimensionless mean kinematic vorticity number (Wm). Within a ductile flow, the non-coaxial component of deformation, defined vorticity, can be normalized to the stretching along the strain axes in order to obtain a dimensionless number that allows to compare the different types of flow. In this way it is possible to define the kinematic vorticity number as $Wk = W/|d2-d3|$ (Passchier, 1987). W represents the vorticity and d2-d3 represents the difference of stretching along the intermediate and minimum principal strain axes. The mean kinematic vorticity number Wm can be assumed equal to Wk because it represents an average value over the deformation interval during which the structure or fabric formed (Xypolias, 2010; Fossen and Cavalcante, 2017). Wm is therefore a measure of the proportion of pure and simple shear components: $Wm = 0$ for pure shear; $Wm = 1$ for simple shear; $0<Wm<1$ for general shear (Passchier, 1987). Simple and pure shear contribute equally to the flow for a value of Wm = 0.71 (Law et al., 2004; Xypolias, 2010).

The kinematic vorticity analysis was carried out on thin sections oriented parallel to the XZ plane of the finite strain ellipsoid.

It was performed using the S-C' method (Kurz and Northrup, 2008), which is based on the measurement of the orientation of C' planes (Fig. 7a) with respect to the shear zone boundary. In any type of flow it is possible to recognize two lines, defined as flow apophyses (A1 and A2), along which the particles do not undergo rotation. The component of simple shear decreases with the angle between the two apophyses: the flow apophyses are orthogonal for pure shear flow, and coincide with each other for simple shear flow. For general shear flow A1 and A2 form an acute angle in the direction of the flow (Fig. 7a). The C' plane represents the bisector of the angle 2ν between the A1 and A2 flow apophyses (Fig. 7a; e.g. Kurz and Northrup, 2008). The vorticity number can be derived through the relation Wk = cos2ν (Kurz and Northrup, 2008) where ν is the angle between C' and C planes that assumed are parallel to the flow apophysis A2 (Kurz and Northrup, 2008; Gillam et al., 2013). Following the procedure proposed by Gillam et al. (2013), we measured the ν angle since the mylonitic foliation has a constant trend, sub-parallel to the well-defined and mapped shear zone boundaries (Carosi et al., 2016b), in the studied transects.

As each element in a flow tends to rotate, including C' planes, it is necessary to consider the largest value for ν, among those measured, to estimate the initial amplitude of the angle during formation of the C' planes. Gillam et al. (2013) proposed to use an average value of the angle ν for low-strain rocks or in cases where C' planes developed in a late stage of the deformation history and nucleated in a stable orientation, as in this case they underwent little or no rotation after inception. For highly strained rocks deformed in long lasting shear zones the maximum value of ν is preferable because, as demonstrated by Kurz and Northrup (2008), the average value is not representative of the original angle of nucleation of C' planes.

Finite strain analysis has been performed on the XZ section of oriented samples applying the center-to-center method (Fry, 1979). The analysis was performed on samples in which an adequate amount of feldspar porphyroclasts with a similar grain size are present. Feldspar porphyroclasts show a homogeneous distribution in the samples used for the analysis and therefore are in agreement with the fundamental assumption of the method (see Genier and Epard, 2007 for a critical review). The center-to-center analysis was carried out using the software EllipseFit 3.2 (Vollmer, 2005).

The data obtained from strain and vorticity analyses were combined using the equations proposed by Wallis et al. (1993) and Law et al. (2004) to obtain the percentages of shortening and stretching of the shear zone (Fig. 7b).

In order to check the kinematics and the type of deformation of the shear zone we calculated the angles θ, between the maximum Instantaneous Stretching Axis (ISA_{max}) in the horizontal plane and the shear zone boundary, as this parameter appears to be fundamental to distinguish between transpression and transtension, according to Fossen and Tikoff (1993) and Fossen et al. (1994). θ angles larger than 45° are indicative of transtensive deformation while θ angles smaller than 45° are indicative of transpressional deformation.

The calculation was performed using the formula proposed by Xypolias (2010) according to which Wk = sin2θ and consequently θ = (arcsinWk)/2. Results were checked with the software Strain Calculator 3.2 (Holcombe, 2009).

4.2 Results of vorticity and strain analyses

Results of vorticity and strain analyses are reported in table 1, polar histograms used to derive the angle ν are reported in figure 8 and Fry graphs of the XZ section are reported in figure 9. In each of the three transects the estimated Wk values are very similar taking into account the degree of deformation of the samples. In protomylonites (samples: ARG 144, ARG 143, ARG 19) Wk varies from 0.32 to 0.34. In mylonites (samples: ARG 45, ARG 21a, ARG 68, ARG 116, ARG 117, ARG 115) Wk varies between 0.37 and 0.69. In ultramylonites (samples: ARG 35, ARG 101, ARG 37, ARG RCV, ARG 41) Wk is variable between 0.81 and 0.89. It is therefore possible to observe a change in the value of Wk along the deformation gradient toward the center of the shear zone.

Finite deformation analysis, combined with Wk values, allowed to obtain shortening and stretching values quite concordant in all the studied samples: shortening varies from 19% to 37% with an average value of 27%; stretching ranges from 23% to 59% with an average value of 36%. θ varies from 9° in protomylonites to 31° in ultramylonites.

5. Geochronology

In-situ U-Th-Pb analyses were performed with LA-ICP-MS on monazites in five samples (ARG 19, ARG 21, ARG 27, ARG 29, ARG 48b) collected along the deformation gradient of the shear zone along the crest of Costabella del Piz (Fig. 6c). Sample ARG 19 is a protomylonite derived from biotite- and sillimanite-bearing migmatite. Samples ARG21, ARG 27, ARG 29 and ARG 48b are mylonites derived from biotite- and white mica-bearing migmatites.

Dating was performed following the analytical procedure suggested by Montomoli et al. (2013). First, minerals with high relief and high birefringence were located using the optical microscope. Subsequently the samples were polished and C-coated to be inspected using a Scanning Electron Microscope (JEOL JSM IT300LV), at the University of Torino (Italy), which allows to distinguish monazite from zircon. On grains selected for dating (examples reported in figure 10), quantitative chemical analyses, reported in Online Resource 1 (spots reported in figure 11), and compositional maps (Fig. 11) were acquired by using electronic microprobe (JEOL 8200 Super Probe), at the University of Milano (Italy), in order to highlight any compositional zoning.

Monazite grains were analyzed in situ by laser-ablation inductively coupled plasma mass spectrometry (LA–ICP-MS) on 30-μm-thick sections at the CNR–Istituto di Geoscienze e Georisorse U.O. Pavia (Italy) using an Ar–F 193-nm excimer laser (GeolLas 102 from Micro-Las) coupled with a magnetic sector ICP-MS (Element I from Thermo-Finnigan). The full description of the analytical procedures is reported in Paquette and Tiepolo (2007) and Tiepolo (2003). Single analyses were performed by a one-minute acquisition of the background signal followed by recording, for at least 30 seconds, the ablation signal of the masses: ^{202}Hg, $^{204}(Hg+Pb)$, ^{206}Pb, ^{207}Pb, ^{208}Pb, ^{232}Th and ^{238}U. The presence of common Pb was evaluated in each analysis on the basis of the net signal of ^{204}Pb (i.e. subtracted for the interference of ^{204}Hg and background). None of the samples gave ^{204}Pb counts above the background level. However the relatively high Hg signal in the gas blank does not exclude the effective presence of common Pb in the analyzed monazites. Analytical conditions were 10 μm diameter of spot size, 8 J/cm^2 of energy density, and 3 Hz of repetition rate. Time-resolved signals were carefully inspected to verify the presence of perturbations related to inclusions, fractures or mixing of different age domains. Laser-induced elemental fractionation and mass bias were corrected using matrix-matched external monazite standard (Moacir monazite: Cruz et al., 1996; Seydoux-Guillaume et al., 2002a,b) considering the values, re-calibrated for isotopic disequilibrium, reported by Gasquet et al. (2010). Eight to nine external standards were analyzed in each analytical run and only those close to the reference values (at least 4 in each run) were considered in order to reduce errors related to the standard reproducibility (Table 2). The relative standard deviation of the analyses was mostly within 2 % – 4 %. External standards and unknowns were integrated over the same time intervals to ensure the efficient correction of fractionation effects. Data reduction was carried out with the GLITTER® software (van Achterbergh et al., 2001). In order to better estimate the uncertainty affecting the $^{206}Pb/^{238}U$, $^{207}Pb/^{235}U$ and $^{208}Pb/^{232}Th$ isotope ratios, the external reproducibility of the standard was propagated relative to individual uncertainties for the isotope ratios. This procedure was carried out for each analytical run as reported in Horstwood et al. (2003). After this error propagation each analysis is accurate within the quoted errors. Data processing and plotting was done with the macro ISOPLOT/Ex (Ludwig, 2003).

5.1 Characterization of the Monazites

Monazite belongs to the family of orthophosphates with general formula $A(PO_4)$ and is an anhydrous rare earth phosphate (Williams et al., 2007). Monazite is ideal for recording the progress of geological processes, because with its extremely variable composition it reflects the chemical and physical changes of the host rocks and preserves the age of crystallization or growth over long geological periods (Williams et al., 2007). It is ideal for the U-Th-Pb method because it can have large concentrations of U and Th but does not incorporate Pb during its formation.

In systems in which the monazite is associated with garnet it is possible to observe partition phenomena of Y and HREE between these two phases (Williams et al., 2007). After xenotime, garnet is the main mineral that can accommodate HREE and Y in metamorphic rocks and its growth or its destabilization strongly influence the distribution of Y and HREE in metamorphic monazites (Pyle and Spear, 1999; Pyle et al., 2001): during prograde metamorphism Y tends to enter preferentially in garnet while during retro-metamorphism Y tends to enter preferentially in monazite (Pyle and Spear, 1999; Pyle et al., 2001; Williams et al., 2007). The microstructural study, combined with the analysis of the variation of the composition of monazites in deformed rocks, allows to understand in which moment of the deformation history the two phases have grown.

Monazites were analyzed for microstructural position (examples of monazites located in different structural positions are reported in figure 10) and the Y content and zoning highlighted by the compositional maps acquired by electron microprobe. In both protomylonite (ARG 19) and mylonites (ARG 21, ARG 27, ARG 29, ARD 48b) no xenotime crystals have been detected and cores of the monazites have often a lower Y content with respect to the rims. Some monazites have asymmetrical shapes. Monazites in mylonites show irregular and frayed edges with asymmetric rims constituted by allanite ± apatite often developed in extensional sites around the crystals.

5.2 U-Th-Pb results

U-Pb data (Table 3) provide mainly discordant ages, with eight concordant U-Pb ages ranging from 348 to 297 Ma (Fig. 12). Except for ARG 19 protomylonite, ^{206}Pb /^{238}U and ^{208}Pb/^{232}Th data yield more concordant ages (Table 3, Fig. 12). Both ^{206}Pb /^{238}U and ^{208}Pb/^{232}Th ages range mainly from 340 to 320 Ma and define a broad rejuvenation trend from the least deformed sample (ARG 19 protomylonite) to highly sheared samples in the core of the shear zone (Fig. 12).

We did not note a systematic correlation between ages and monazite chemical domains. The oldest U-Th-Pb ages were obtained from a monazite grain included in garnet (>400 Ma; Mnz 59, sample ARG 48b) and a monazite grain included in a deformed white mica (^{206}Pb/^{238}U age of 374 ± 6 Ma; Mnz 9, ARG 29), suggesting a textural control and inheritance of the obtained ages.

6. Discussion

The FMSZ is a steeply dipping shear zone with a main right-lateral reverse top-to-the-SE sense of shear, whereas locally it shows a normal sense of shear, depending on the dip direction of the mylonitic foliation. The FMSZ developed under conditions of decreasing temperature, starting from the HT amphibolite facies to at least the LT amphibolite facies, as suggested by the presence of sillimanite + biotite and biotite + white mica along the protomylonitic and mylonitic foliations, respectively. The geometry of the foliation and mineral lineation as well as the kinematic indicators are concordant in the protomylonites and in the mylonites. Temperature during Alpine deformation was 375 ± 30 °C (greenschist facies metamorphism; Corsini et al., 2004; Sanchez et al., 2010) and, as a consequence, the amphibolite-facies metamorphism may be inferred to be pre-Alpine.

The results allowed us to define for the first time the deformation regime and the finite strain of the FMSZ.

The kinematic vorticity data obtained by the S-C' method (Kurz and Northrup, 2008) allowed us to quantify the deformation, characterized by a non-coaxial flow, in terms of percentage of pure and simple shear components.

Samples from the less deformed lithotypes, localized in the external portion of the shear zone, record a deformation dominated by pure shear. The amount of simple shear increases towards the center of the shear zone, from ~24 % in the protomylonites to ~ 62% in the ultramylonites (Fig. 13a). Finite strain analysis yields average shortening and stretching values of 27 % and 36 %, respectively.

Taking into account the type of flow, the finite strain and the angles θ between the maximum horizontal ISA and the shear zone boundaries (Fig. 13b), we can recognize a change from a pure shear dominated transpression to a simple shear dominated transpression (Fig. 13c) according to the models proposed by Fossen and Tikoff (1993) and by Fossen et al. (1994). The attitude of the mylonitic foliation is sub-vertical along the 20 km length of the shear zone, in accordance with a transpressive shear zone setting (Fossen et al., 1994; Fossen, 2016). In the case of transtensional deformation as suggested by Musumeci & Colombo (2002), the attitude of mylonitic foliation is expected to be sub-horizontal due to the main sub-vertical shortening direction. Iacopini et al. (2008), discussing the orientations of the elongation lineation, suggest two kinds of transpressive shear zones: in the case of a sub-vertical lineation the shear zone was subjected to vertical extrusion while in the case of a sub-horizontal lineation extrusion was horizontal. The elongation lineation within the FMSZ is gently plunging, thus it would be compatible with a sub-horizontal direction of extrusion. Extrusion and shear zones with a component of pure shear are generally subjected to strain compatibility problems (Hudleston, 1999) and it is not trivial to explain how the flattening component of the deformation is accommodated.

To fix this problem Ramsay and Huber (1987) and Hudleston (1999) suggested that the flattening component can be obtained in a simple shear regime by volume loss in the deforming material. In this way the strain compatibility is maintained. However, this is not the case of the FMSZ because there is no evidence of structures suggesting major volume loss in the deformed rocks and the kinematic vorticity analysis revealed a major component of pure shear during deformation.

Anyway, according to Fossen (2016) strain compatibility problems are also overcome if the wall rocks are deformed by the same amount of coaxial strain as the shear zone. The wall rocks of the FMSZ, i.e. the GSV and the TMC complexes are deformed by open to tight upright folds with axial planes parallel to the mylonitic foliation in the FMSZ. According to Carosi et al. (2016b) and Simonetti et al. (2017) these upright folds accommodate the component of shortening perpendicular to the FMSZ. According to this, the wall rocks and the shear zone could stretch together with no strain compatibility problems.

The Argentera-Mercantour Massif was involved in the Alpine orogeny at ~22 Ma (Corsini et al., 2004, Sanchez et al., 2011). Most of the Alpine deformation is concentrated in the sedimentary covers, detached from the metamorphic basement along gypsum and limestone breccias levels (Malaroda et al., 1970), in which several folding phases are recognizable (d'Atri et al., 2016; Barale et al., 2016). Evidence of Alpine deformation in the basement are brittle/ductile strike-slip faults and top-to-the-S reverse shear zones developed under greenschist facies conditions during the lower Miocene (Corsini et al., 2004; Baietto et al., 2009). Variscan HT foliation and mylonitic foliation in the FMSZ all along its length are always subvertical and are not affected by strong subsequent folding.

U-Th-Pb geochronology on monazites provides no Alpine ages showing that the shear zone was not significantly reactivated during the Alpine orogeny. U-Pb data are discordant whereas the $^{206}Pb/^{238}U$ and $^{208}Pb/^{232}Th$ ages show a better concordance. As recently demonstrated by Erickson et al. (2015), the perturbation of the U-Th-Pb systematics of monazite can be caused by intracrystalline deformation. We interpret the obtained geochronological data combining textural observations, monazite chemistry and age distribution. The oldest U-Th-Pb ages were obtained from monazite grains included in garnet (Fig. 10a) and within a deformed white mica (Fig. 10b). These grains probably escaped subsequent deformation and other events perturbating the U-Th-Pb systematics. They can be interpreted as inherited ages from older tectono-metamorphic events as previously documented by other authors (Monié and Maluski 1983; Rubatto et al. 2001; Corsini et al. 2004).

The $^{206}Pb/^{238}U$ and $^{208}Pb/^{232}Th$ ages range mainly from about 340 to 320 Ma. The oldest $^{206}Pb/^{238}U$ ages of this range were obtained in monazites along the protomylonitic foliation (Fig. 10c) close to the margin of the shear zone.

This age, according to the syn-kinematic mineral assemblage and to the main deformation mechanism of quartz and feldspar, suggests that Variscan shear deformation in the Argentera-Mercantour Massif started at the metamorphic peak (dated at ~340 Ma in the GSV complex, Compagnoni et al., 2010; Rubatto et al., 2010) or shortly after it during the first partial melting event and triggered the exhumation of the GSV complex.

Both $^{206}Pb/^{238}U$ and $^{208}Pb/^{232}Th$ ages become younger along the deformation gradient (Fig. 14) and monazite grains along the mylonitic foliation in the core of the shear zone (Fig. 10d) show $^{206}Pb/^{238}U$ and $^{208}Pb/^{232}Th$ ages of ~320 ± 6 Ma. This broad correlation between ages and deformation gradient suggests a progressive concentration of deformation into the center of the shear zone.

This is in agreement with the type II shear zone growth-model proposed by Fossen (2016). Here deformation localizes in the central part because of strain softening. Thus, the margins become inactive and preserve the features acquired during the early stages of shearing while the active part gets progressively thinner (Fig. 15) and records the final stages of shearing. The result is a shear zone with a deformation gradient toward the central part along which, as in the case of the FMSZ, it is possible to observe variations in temperature, age of deformation and deformation regime (Fig. 13d). The occurrence of allanite ± apatite rims around monazites in mylonites is indicative of the breakdown of monazite during retrograde metamorphism. Since allanite and apatite grew asymmetrically in extensional sites around the monazite crystals, in agreement with the orientation of the instantaneous stretching axis during dextral shearing, it is possible to state that this reaction took place synkinematically during retrograde metamorphism (Gibson et al., 2004) and testify the further decrease in temperature during a late stage of shearing.

In the Alpine External Crystalline Massifs Variscan shear deformation has never been characterized in terms of vorticity of the flow, and its age, considered to be between ~320 Ma and ~300 Ma (Bussy and Von Raumer, 1993; Genier et al., 2008; Guillot et al., 2009) or Late Visean (Musumeci and Colombo, 2002), was always inferred relying on the age of emplacement of sin-kynematic granites. Ages of ~340 Ma obtained in this work are in agreement with the age proposed by Musumeci and Colombo (2002). Ages of ~320 Ma are consistent with both magmatic ages present in literature and ages of the dextral transpressional deformation in the Maures-Tanneron Massif (Schneider et al., 2014) and Corsica-Sardinia (Carosi and Palmeri, 2002; Di Vincenzo et al., 2004; Iacopini et al., 2008), dated at ~320-310 Ma (U-Th-Pb on monazites, Carosi et al., 2012), that affects migmatitic crust with strong tectono-metamorphic similarities with the migmatites cropping out in the Argentera-Mercantour Massif. If we restore the counterclockwise Oligo-Miocenic rotation of the Corsica-Sardinia block (Vigliotti and Kent, 1990; Todesco and Vigliotti, 1993, Advokaat et al., 2014) and of the Western Alps (Thomas et al., 1999; Collombet et al., 2002; Maffione et al., 2008), the three studied sectors lie in lateral continuity and show a similar structural and metamorphic evolution. Shear deformation recognized in northern Sardinia has been attributed to a network of dextral shear zones belonging to the East Variscan Shear Zone (EVSZ; Corsini and Rolland, 2009; Carosi et al., 2012; Schneider et al., 2014). The FMSZ can be considered as a branch of EVSZ. In the Argentera-Mercantour Massif dextral shear deformation started at ~340 Ma under amphibolite-facies conditions. In the Maures-Tanneron Massif an anatectic post-collisional event is reported at ~340 Ma (Schneider et al., 2014; Oliot et al., 2015) while in northern Sardinia collision-related MP - MT metamorphism has been recognized at 344 ± 7 Ma (Rb-Sr method; Ferrara et al., 1978), although older ages of the thickening stage also occur in Sardinia and Corsica (between 380 and 340 Ma; Oliot et al., 2015). Although the different sectors of the southern European Variscan Belt record a similar tectono-metamorphic evolution (Corsini and Rolland, 2009), the age of shearing along the EVSZ is diachronous, and this is the first time that an age of ~340 Ma is obtained for amphibolite-facies mylonitic deformation linked to this regional-scale system of shear zones. The different sectors of the belt are affected by orogen parallel dextral transpression (Carosi and Palmeri, 2002) at different time because of the progressive change of orientation of the belt with respect to the regional stress field (Carosi et al., 2012). This is also confirmed by the increase of the simple shear component of the deformation recognized both in Sardinia (Carosi and Palmeri, 2002), and, for the first time, in the Argentera-Mercantour Massif. Our data are therefore in agreement with the occurrence of a shear belt in the eastern sector of the Variscan Belt (Fig. 16).

Our new structural data support the model proposed by Rollet et al. (2002), Rosenbaum et al. (2002) and Advokaat et al. (2014) of the Corsica-Sardinia Block connected to southern France and in continuity with the Western Alps since all these sectors of the Variscan Belt show structural and lithological similarities, in contrast to reconstructions of the Variscan framework which show Corsica and/or Sardinia in a more westerly position connected to Spain (e.g., Fig. 8 in von Raumer et al., 2013).

In the western sector of the Iberian Massif, syn-anatectic sinistral transpressive deformation is recognized and dated at ~340 Ma using monazite and zircon (Pereira et al., 2008; 2010), therefore contemporary with the onset of shear deformation in the External Crystalline Massifs. Shearing in this sector of the belt is interpreted to be due to the formation of the Ibero-Armorican Arc. The presence of a contemporary system of shear zones with opposite kinematics in the western and eastern sector of the belt suggests that, as proposed by Matte (1986a,b), Garcia-Navarro and Fernandez (2004) and Pereira et al. (2008), the European Variscan Belt formed and evolved in a manner analogous to the indentation model proposed by Tapponier and Molnar (1977) and Tapponier et al. (1982). Our data are in agreement with a composite orocline model already proposed by Matte (1986a,b, 2001), Corsini and Rolland (2009), Guillot et al. (2009) and Carosi et al. (2012) with a western arc, still preserved, and an eastern arc that is truncated by the EVSZ.

Our data support that the FMSZ is not a minor shear zone confined to one tectonic unit, but it is part of a large-scale system of shear zones that, because of its long-lasting activity, length and thickness, may have played a primary role in the exhumation of migmatitic rocks during Variscan time. Goscombe and Gray (2009) demonstrate that maximum stretching directions do not necessarily correlate with the flow vectors experienced during orogenesis. Although the stretching lineation in the FMSZ is shallowly inclined, the material flow may have had a large vertical component.

7. Conclusive remarks

The data obtained in this work allow us to establish that:

- the FMSZ is a dextral transpressional shear zone characterized by a non-coaxial flow with a component of pure shear and a component of simple shear, the latter increasing toward the central and most strained part of the shear zone;

- the FMSZ initiated during high-temperature amphibolite facies metamorphism and evidence of it is preserved in protomylonites and mylonites;

- Alpine deformation in the Argentera-Mercantour Massif occurred as local reactivation of Variscan structure and as localized reverse top-to-the-S shear zones, developed under greenschist facies conditions, cross-cutting the FMSZ mylonites;

- shear deformation started at ~ 340 Ma, near the metamorphic peak recorded in the GSV complex or shortly after it, and progressively migrated toward the core of the shear zone in a time span of ~10-20 Ma. In the same time interval a gradual change in the deformation regime is observed;

- microstructural and geochronological analysis constrain a type II evolution for this shear zone that can be a good example of strain softening within a regional-scale shear zone.

- the FMSZ is a sector of a system of regional-scale dextral shear zones occurring in the eastern sector of the Variscan Belt (EVSZ) at 320-310 Ma;

- shear deformation did not begin synchronously in all the part of the EVSZ but initiated earlier in its NE part and then propagated to the SW.

Software

The data processing of the geochronological study was performed using the software GLITTER® (Macquarie Research Ltd 2001; Van Achterbergh et alii, 2001). The finite strain analysis was performed using the software EllipseFit 3.2 by Vollmer (2015). Calculation of the θ angle was performed using the software Strain Calculator 3.2 by Holcombe (2009).

Acknowledgements

Research supported by funds from Torino University (Ricerca Locale 2014, 2015), Pisa University (PRA 2016) and PRIN 2016 (prot. 2015EC9PJ5_004; resp. R Carosi and C. Montomoli). We thank Michel Corsini and an anonymous reviewer for their careful revision that significantly improved the quality of the manuscript.

References

Advokaat E. L., van Hinsbergen D. J. J., Maffione M., Langereis C. G., Vissers R. L. M., Cherchi A., Schroeder R., Madani H., Columbu S., 2014, Eocene rotation of Sardinia, and the paleogeography of the western Mediterranean region. Earth Planet. Sci. Lett., 401, 183–195, doi:10.1016/j.epsl.2014.06.012.

Arthaud F., Matte P., 1977, Late Paleozoic strikeslip faulting in southern Europe and northern Africa: results of a right-lateral shear zone between the Appalachians and Urals. Geological Society of America Bulletin, 88, 1305–1320.

Baietto A., Perello P., Cadoppi P., Martinotti G., 2009, Alpine tectonic evolution and thermal water circulations of the Argentera Massif (South-Western Alps). Swiss Journal of Geosciences 102 (2), 223 - 245.

Ballèvre M., Bosse V., Ducassou C., Pitra P., 2009, Palaeozoic history of the Armorican Massif: models for the tectonic evolution of the suture zones. Comptes Rendus Geoscience, 341, 174–201.

Barale L., Bertok C., D'atri A., Martire L., Piana F., Domini G., 2016, Geology of the Entracque–Colle di Tenda area (Maritime Alps, NW Italy). Journal of Maps, 12, 359–370.

Bellot J.-P., 2005, The Palaeozoic evolution of the Maures massif (France) and its potential correlation with other areas of the Variscan belt: a review, in: Carosi R., Dias R., Iacopini D. & Rosenbaum G. (Eds.). The southern Variscan belt. Journal of the Virtual Explorer, Electronic Edition, ISSN, 19, 1441-8142.

Brun J.P, Burg J.P, 1982, Combined thrusting and wrenching in the Ibero-Armorican arc: A corner effect during continental collision. Earth and Planetary Science Letters, 61, 2, 319-332.

Burg J.-P., Matte P., 1978, A cross section through the French Massif Central and the scope of its Variscan Geodynamic Evolution. Zeitschrift der Deutschen Geologischen Gesellschaft, 129, 429–460.

Bussy F., Von Raumer J., 1993, U-Pb dating of Paleozoic events in the Mont Blanc Cristalline Massif, Western Alps. Terra Abstract EUG07, Strasbourg, 382-3.

Carosi R., Palmeri R., 2002, Orogen-parallel tectonic transport in the Variscan belt of northeastern Sardinia (Italy): implications for the exhumation of medium-pressure metamorphic rocks. Geol. Mag., 139, 497 - 511.

Carosi R., Frassi C., Iacopini D., Montomoli C., 2005, Post-collisional transpressive tectonic in northern Sardinia. In: Carosi, R., Dias, R., Iacopini, D., Rosenbaum, G. (Eds.), The Southern Variscan Belt, Electronic Edition. J. Virt. Expl. 1441-8142, vol. 19. Paper 4.

Carosi R., Montomoli C., Rubatto D., Visonà D., 2006, Normal-sense shear zones in the core of the Higher Himalayan Crystallines (Bhutan Himalayas): evidence for extrusion? In: LAW, R. D., SEARLE, M. P. & GODIN, L. (eds) Channel Flow, Ductile Extrusion and Exhumation in Continental Collision Zones. Geological Society, London, Special Publications, 268, 425-444.

Carosi R., Montomoli C., Visonà D., 2007, A structural transect in the Lower Dolpo: Insights on the tectonic evolution of western Nepal: Journal of Asian Earth Sciences, v. 29, p. 407-423.

Carosi R., Montomoli C., Rubatto D., Visonà D., 2010, Late Oligocene high-temperature shear zones in the core of the Higher Himalayan Crystallines (Lower Dolpo, western Nepal). Tectonics, 29, TC4029, doi: 10.1029/2008TC002400.

Carosi R., Montomoli C., Tiepolo M., Frassi C., 2012, Geochronological constraints on post-collisional shear zones in the Variscides of Sardinia (Italy), Terra Nova, 24, 42 - 51.

Carosi R., Montomoli C., Iaccarino S., Massonne H. J. Rubatto D., Langone A., Gemignani L., Visonà D., 2016a, Middle to late Eocene exhumation of the Greater Himalayan Sequence in the Central Himalayas: Progressive accretion from the Indian plate. Geological Society of America Bullettin, 128, 9 - 10, doi: 10.1130/B31471.1.

Carosi R., D'addario E., Mammoliti E., Montomoli C., Simonetti M., 2016b, Geological map of the northwestern portion of the Ferriere-Mollieres shear zone, Argentera Massif, Italy. Journal of Maps, 12, 466-475.

Carrapa B., Wijbrans J., Bertotti G., 2003, Episodic exhumation in the Western Alps, Geology, 31, 7, 601– 604.

Challandes N., Marquer D., Villa I.M., 2003, Dating the evolution of C-S microstructures: a combined ^{39}Ar -^{40}Ar step-heating and UV laserprobe analysis of the Alpine Roffna shear zone. Chemical Geology 197 (1–4), 3–19.

Challandes N., Marquer D., Villa I., 2008, P–T-tmodelling, fluid circulation, and ^{39}Ar-^{40}Ar and Rb–Sr mica ages in the Aar Massif shear zones (Swiss Alps). Swiss Journal of Geosciences 101 (2), 269–288.

Collombet M., Thomas J. C.,. Chauvin A, Tricart P., Bouillin J. P., Gratier J. P., 2002, Counterclockwise rotation of the western Alps since the Oligocene: New insights from paleomagnetic data. Tectonics, 21, 4, 1032, doi:10.1029/2001TC901016.

Compagnoni R., Ferrando S., Lombardo B., Radulesco N., Rubatto D., 2010, Paleo-European crust of the Italian Western Alps: Geological history of the Argentera Massif and comparison with Mont Blanc-Aiguilles Rouges and Maures-Tanneron Massifs. In: (Eds.) M. Beltrando, A. Peccerillo, M. Mattei, S. Conticelli & C. Doglioni, Journal of the Virtual Explorer, volume 36, paper 4, doi: 10.3809/jvirtex.2009.00228

Corsini M., Ruffet G., Caby R., 2004, Alpine and late Hercynian geochronological constraints in the Argentera Massif (Western Alps). Eclogae geologicae Helvetiae, 97, 3 - 15.

Corsini M., Rolland Y., 2009, Late evolution of the southern European Variscan belt: exhumation of the lower crust in a context of oblique convergence. Comptes Rendus Geosciences 341 (2–3), 214–223.

Cottle J.M., Searle M.P., Jessup M.J., Crowley J.L., Law R.D., 2015, Rongbuk Re-visited: Geochronology of Leucogranites in the Footwall of the South Tibetan Detachment System, Everest Region, Southern Tibet. Lithos, 227, 94 - 106.

Cruz M.J., Cunha J.C., Merlet C., Sabatè P., 1996, Datação pontual das monazitas da região de Itambé, Bahia, através da microssonda electronica XXXIX Congresso Brasileiro de Geologia, vol. 2, Sociedade Brasileira de Geologià-Núcleo, Bahià-Segipe, 206–209.

d'Atri A., Piana F., Barale L., Bertok C., Martire L., 2016, Geological setting of the southern termination of Western Alps. Int J Earth Sci (Geol Rundsch), 105, 1831–1858. DOI 10.1007/s00531-015-1277-9.

Dias R., Ribeiro A., The Ibero-Armorican Arc: a collision effect against an irregular continent?. Tectonophysics 246, 113-128.

Dias R., Ribeiro A., Romão J., Coke C., Moreira N., A review of the arcuate structures in the Iberian Variscides; constraints and genetic models. Tectonophysics 681, 170-194.

Di Vincenzo G., Carosi R., Palmeri R., 2004, The relationship between tectono-metamorphic evolution and argon isotope records in white mica: constraints from in situ ^{40}Ar–^{39}Ar laser analysis of the Variscan basement of Sardinia. Journal of Petrology 45, 5, 1013-1043.

Di Vincenzo G., Carosi R., Palmeri R., Tiepolo M., 2007, A comparative U-Th-Pb (zircon-monazite) and ^{40}Ar- ^{39}Ar (muscovite-biotite) study of shear zones in northern Victoria Land (Antarctica): Implications for geochronology and localized reworking of the Ross Orogen. Journal of Metamorphic Geology, 25, 605- 630.

Dunlap W., Teyssier C., McDougall I., Baldwin S., 1991, Ages of deformation from K/Ar and ^{40}Ar/^{39}Ar dating of white micas. Geology 19, 1213–1216.

Erickson T.M., Pearce M.A., Taylor R.J.M., Timms N.E., Clark C., Reddy S.M., Buick I.S., 2015, Deformed monazite yields high-temperature tectonic ages: Geology, 43, 383–386, doi: 10.1130/G36533.1.

Faure-Muret A., 1955, Etudes géologiques sur le massif de l'Argentera-Mercantour et ses enveloppes sédimentaires. Mémoires pour servir à l'explication de la Carte géologique détaillée de la France, Paris, Imprimerie Nationale, France, with «Esquisse Géologique du Massif de l'Argentera-Mercantour et de sa Bordure Sédimentaire (Versant français) » at the 1/100.000 scale., pp 336.

Faure M., Lardeaux J. M., Ledru, P., 2009, A review of the pre-Permian geology of the Variscan French Massif Central. Comptes Rendus Geosciences, 341, 202–213.

Fernàndez-Lozano J., Pastor-Galàn D., Gutiérrez-Alonso G., Franco P., New kinematic constraints on the Cantabrian orocline: A paleomagnetic study from the Peñalba and Truchas synclines, NWSpain. Tectonophysics, 681, 195-208.

Ferrara G., Ricci C. A., Rita F., 1978, Isotopic ages and tectono-metamorphic history of the metamorphic basement of north-eastern Sardinia. Contributions to Mineralogy and Petrology 68, 99 - 106.

Ferrando S., Lombardo B., Compagnoni R., 2008, Metamorphic history of HP mafic granulites from the Gesso-Stura Terrain (Argentera Massif, Western Alps, Italy). European Journal of Mineralogy, 20, 777 - 790.

Festa V., Prosser G., Caggianelli A., Grande A., Langone A., Mele D., 2016, Vorticity analysis of the Palmi shear zone mylonites: new insights for the Alpine tectonic evolution of the Calabria-Peloritani terrane (southern Italy). Geological Journal 51:670–681. doi: 10.1002/gj.2673.

Fluck P., Piqué A., Schneider J. L., Whitechurch H., 1991., Le socle vosgien. Sciences Géologiques, 44, 207–235.

Fossen H., Tikoff B., 1993, The deformation matrix for simultaneous simple shearing, pure shearing and volume change, and its application to transpression-transtension tectonics. Journal of Structural Geology, 15, 413-422, DOI: 10.1016/0191-8141(93)90137-Y.

Fossen H., Tikoff B., Teyssier C., 1994, Strain modeling of transpressional and transtensional deformation. Norsk Geol. Tidsskr. 74, 134-145.

Fossen H., 2016, Structural Geology. Cambridge University Press, p 510.

Fossen H., Cavalcante G. C. G., 2017, Shear zones – A review. Earth-Science Reviews, 171, 434–455.

Franke W., 1989, Tectonostratigraphic units in the Variscan belt of central Europe. In: Dallmeyer, R. D. (ed.) Terranes in the Circum-Atlantic Paleozoic Orogens. Geological Society of America Special Papers, 230, 67–90.

Franke W., Robin L. M. C., Torsvik T. H., 2017, The Palaeozoic Variscan Oceans Revisited. Gondwana Research, 48, 257-284. doi: 10.1016/j.gr.2017.03.005.

Fry N., 1979, Random point distribution and strain measurement in rocks. Tectonophysics, 60, 89-105.

Garcia-Navarro E., Fernandez C., 2004, Final stages of the Variscan orogeny at the southern Iberian massif: Lateral extrusion and rotation of continental blocks. Tectonics, 23, tc6001, doi:10.1029/2004tc001646.

Gasquet D., Bertrand J.M., Paquette J.L., Lehmann J., Ratzoy G., De Ascencão Guedes R., Tiepolo M., Boullier A.M., Scaillet S., Nomade S., 2010, Miocene to Messinian deformation and hydrothermal activity in a pre-Alpine basement massif of the French western Alps: new U–Th–Pb and argon ages from the Lauzière massif. Bulletin de la Société Géologique de France, 181, 227–241.

Genier F., Epard J.L., 2007, the Fry method applied to an augen orthogneiss: problems and results. Journal of structural geology, 29, 209-244.

Genier F., Bussy F., Epard J.L., Baumgartner L., 2008, Water-assisted migmatization of metagraywackes in a Variscan shear zone, Aiguilles-Rouges Massif, western Alps: Lithos, v. 102, p. 575–597.

Gibson H.D., Carr S.C., Brown R.L., Hamilton M.A., 2004, Correlations between chemical and age domains in monazite, and metamorphic reactions involving major pelitic phases: an integration of ID-TIMS and SHRIMP geochronology with Y–Th–U X-ray mapping. Chemical Geology, 211, 237–260.

Gillam B. G., Little T. A., Smith E., Toy V. G., 2013, Extensional shear band development on the outer margin of the Alpine mylonite zone, Tatare Stream, Southern Alps, New Zealand. Journal of Structural Geology, 54, 1-20.

Goscombe B. D., Hand M., Gray D., Mawby J., 2003, The metamorphic architecture of a transpressional orogen: The Kaoko Belt, Namibia. J. Pet. 44, 679-711.

Goscombe B., David G., Richard A., David A. F., James V., 2005, Event geochronology of the Pan-African Kaoko Belt, Namibia. Precambrian Research, 140, 103.e1–103.e41.

Goscombe B. D., Grey D. R., 2009, Metamorphic response in orogens of different obliquity, scale and geometry. Gondwana Reserch, 15, 2, 151-167.

Guillot S., Ménot R.P., 2009, Paleozoic evolution of the Extern Crystalline Massifs of the Western Alps. C.R. Geosciences, 341, 253–265.

Guillot S., Di Pola S., Ménot R. P., Ledru P., Spalla M. I., Gosso G., Schwartz S., 2009, Suture zone and importance of strike-slip faulting for Variscan geodynamic reconstructions of the External Crystalline Massifs of the Western Alps. Bulletin de la Société Géologique de France, 180, 6, 483–500.

Holcombe R., 2009, RJH StrainCalculator 3.2.

Horstwood M.S.A., Foster G.L., Parrish R.R., Noble S.R., Nowell G.M., 2003, Common-Pb corrected in situ U-Pb accessory mineral geochronology by LA-MCICP-MS: Journal of Analytical Atomic Spectrometry,18, 837–846.

Hudleston P., 1999, Strain compatibility and shear zones: is there a problem? Journal of Structural Geology, 21, 923–932.

Iaccarino S., Montomoli C., Carosi R., Massonne H.-J., Langone A., Visonà D., 2015, Pressure-temperature-time-deformation path of kyanite-bearing migmatitic paragneiss in the Kali Gandaki valley (central Nepal): Investigation of late Eocene–early Oligocene melting processes: Lithos, v. 231, p. 103–121, doi: 10.1016 /j .lithos .2015.06 .005 .

Iaccarino S., Montomoli C., Carosi R., Massonne H.-J., Visonà D., 2017, Geology and tectono-metamorphic evolution of the Himalayan metamorphic core: insights from the Mugu Karnali transect, Western Nepal (Central Himalaya). Journal of Metamorphic Geology, 35, 3, 301-325.

Iacopini D., Carosi R., Montomoli C., Passchier C. W., 2008, Strain analysis of flow in the Northern Sardinian Varisican Belt: recognition of a partitioned oblique deformation event. Tectonophysics, 221, 345 - 359.

Iacopini D., Carosi R., Xypolias P., 2010, Implications of complex eigenvalues in homogeneous flow: a three-dimensional kinematic analysis. Journal of Structural Geology, 32, 1, 93-106.

Iacopini D., Frassi C., Carosi R., Montomoli C., 2011, Limits and biases on the three-dimensional vorticity analysis using porphyroblast system: a discussion and application to natural example, In: Deformation Mechanism, Rheology & Tectonics: Microstructures, Mechanics & Anisotropy, Special issue, 2011, Special Publication - Geological Society of London, 360, 301-318.

Kohn M. J., Wielnad M., Parkinson C. D., Upreti B. N., 2005, Five generations of monazite in Langtang gneisses: Implication for chronology of the Himalayan metamorphic core. Journal of Metamorphic Geology, 23, 399 - 406.

Kohn M.J., 2008, P-T-t data from Nepal support critical taper and repudiate large channel flow of the Greater Himalayan Sequence: Geological Society of America Bulletin, 120, 259–273.

Kurz G.A., Northrup C.J., 2008, Structural analysis of mylonitic fault rocks in the Cougar Creek Complex, OregoneIdaho using the porphyroclast hyperbolic distribution method, and potential use of SC’-type extensional shear bands as quantitative vorticity indicators. Journal of Structural Geology 30, 1005-1012.

Larson K. P., Cottle M. J., 2015, Initiation of crustal shortening in the Himalaya. Terra Nova, 27, 169 - 174.

Larson K.P., Godin L., 2009, Kinematics of the Greater Himalayan Sequence, Dhaulagiri Himal: Implications for the structural framework of central Nepal: Journal of the Geological Society, 166, 25-43.

Law R. D., Searle M. P., Simpson R. L., 2004, Strain, deformation temperatures and vorticity of flow at the top of the Greater Himalayan Slab, Everest Massif, Tibet. Journal of the Geological Society, London, 161, 305-320

Li P., Sun M., Rosenbaum G., Cai K., Chen M., He Y., 2016, Transpressional deformation, strain partitioning and fold superimposition in the southern Chinese Altai, Central Asian Orogenic Belt (Article). Journal of Structural Geology, 87, 64-80.

Ludwig K.R., 2003, Isoplot/Ex Version 3.0: A Geochronological Toolkit for Microsoft Excel: Berkeley Geochronology Center Special Publication, 4, 74 pp.

Maffione M., Speranza F., Faccenna C., Cascella A., Vignaroli G., Sagnotti L., 2008, A synchronous Alpine and Corsica-Sardinia rotation. J. Geophys. Res., 113, B3, doi:10.1029/2007JB005214.

Malaroda R., Carraro F., Dal Piaz G. V., Franceschetti B., Sturani C., Zanella E., 1970, Carta geologica del Massiccio dell'Argentera alla scala 1:50.000 e note illustrative. Memorie della Società Geologica Italiana. Volume 9, 557 - 663.

Matte P., Ribeiro A., 1975, Forme et orientation de l’ellipsoïde de déformation dans la virgation hercynienne de Galice. Relations avec le plissement et hypothèses sur la genèse de l’arc ibéro-armoricain. CR Acad. Sci. Paris, 280, 2825–2828.

Matte P., 1986a, La Chaîne varisque parmi les chaînes paléozoïques péri-atlantiques, modèle d’évolution et position des grands blocs continentaux au Permo-Carbonifère. Bull. Soc. Geol. France 8, 4 - 24.

Matte, P., 1986b. Tectonics and plate tectonics model for the Variscan belt of Europe. Tectonophysics, 126, 329 - 374.

Matte, P., 2001, The Variscan collage and orogeny (480–290 Ma) and the tectonic definition of the Armorica microplate: a review: *Terra nova*, 13, p. 122–128.

Monié P., Maluski H., 1983, Données géochronologiques ^{39}Ar/^{40}Ar sur le socle ante Permien du massif de l’Argentera-Mercantour (Alpes-Maritimes, France). Bull. Soc. Géol. France 7, 247–257.

Montomoli C., Iaccarino S., Carosi R., Langone A., Visonà D., 2013, Tectonometamorphic discontinuities within the Greater Himalayan Sequence in western Nepal (central Himalaya): Insights on the exhumation of crystalline rocks. Tectonophysics, 608, 1349 - 1370.

Montomoli C., Carosi R., Iaccarino S., 2015, Tectonometamorphic discontinuities in the Greater Himalayan Sequence: A local or a regional feature? In Mukherjee, S., Carosi, R., van der Beek, P.A., Mukherjee, B.K., and Robinson, D.M., eds., Tectonics of the Himalaya: Geological Society of London Special Publication 412, 25 - 41, doi: 10 .1144 /SP412 .3.

Mulch A., Cosca M.A., 2004. Recrystallization or cooling ages: in situ UV-laser ^{40}Ar/^{39}Ar geochronology of muscovite in mylonitic rocks. Journal of the Geological Society, London 161 (4), 573–582.

Musumeci G., Colombo F., 2002, Late Visean mylonitic granitoids in the Argentera Massif (Western Alps): age and kinematic constraints on the Ferrière-Mollières shear zone. Comptes Rendus de l'Académie des Sciences Serie II 334, 213 - 220.

Nabavi S. T., Diaz-Azpiroz M., Talbot C.J., 2016, Inclined transpression in the Neka Valley, eastern Alborz, Iran. Int J Earth Sci (Geol Rundsch), doi: 10.1007/s00531-016-1388-y.

Oliot, E., Melleton, J., Schneider, J., Corsini, M., Gardien, V. and Rolland, Y., 2015. Variscan crustal thickening in the Maures-Tanneron massif (South Variscan belt, France): new in situ monazite U-Th-Pb chemical dating of high-grade rocks: Bulletin de la Société géologique de France, 186, p. 145–169, doi: 10.2113/gssgfbull.186.2-3.145.

Padovano M., Elter F. M., Pandeli E., Franceschelli M., 2012, The East Variscan Shear Zone: new insights into its role in the Late Carboniferous collision in southern Europe. International Geology Review, 54, 957–970.

Padovano M., Dörr W., Elter F. M., Gerdes A., 2014, The East Variscan Shear Zone: Geochronological constraints from the Capo Ferro area (NE Sardinia, Italy). Lithos,196-197, 27-41.

Paquette J.L., Tiepolo M., 2007. High resolution (5 μm) U–Th–Pb isotope dating of monazite with excimer laser ablation (ELA)–ICPMS. Chemical Geology, 240, 222–237.

Passchier C.W., 1987, Stable position of rigid objects in non-coaxial flow: a study in vorticity analysis. Journal of Structural Geology, 9, n° 5/6, pp 679-690.

Passchier C.W., 1991, The classification of dilatant flow type. Journal of Structural Geology, 13, 101-104.

Passchier C.W., Trouw R.A.J., 2005, Microtectonics, Springer-Verlag Berlin Heidelberg, p 101.

Pereira M.F., Arturo Apraiz A., Silva J.B., Chichorro M., 2008, Tectonothermal analysis of high-temperature mylonitization in the Coimbra–Córdoba shear zone (SW Iberian Massif, Ouguela tectonic unit, Portugal): evidence of intra-continental transcurrent transport during the amalgamation of Pangea. Tectonophysics 461, 378–394.

Pereira M.F., Silva J.B., Drost K., Chichorro M., Apraiz A., 2010,. Relative timing of transcurrent displacements in northern Gondwana: New U–Pb laser ablation MS–ICP–MS zircon and monazite geochronology of gneisses and sheared granites from the Western Iberian Massif (Portugal). Gondwana Research 17 (2–3), 461–481.

Piazolo S., Passchier C. W., 2002, experimental modelling of viscous inclusions in a circular high-strain ring: implication for the interpretation of shape fabrics and deformed enclaves. J Geophy Res, 107, B10, 2242, ETG 11: 1 - 15.

Platt J., Vissers R., 1980, Extensional structures in anisotropic rocks. Journal of Structural Geology 2, 397-410.

Pyle J. M., Spear F. S., 1999, Yttrium zoning in garnet: coupling of major and accessory phases during metamorphic reactions. Geol. Mat. Res. 1, 1 - 49

Pyle J. M., Spear F. S., Rudnick R. L., Mcdonough W. F., 2001, Monazite-xenotime-garnet equilibrium in metapelites and a new monazite-garnet thermometer. J. Petrol., 42, 2083–10.

Rolin P., Marquer D., Colchen M., Cartannaz C., Cocherie A., Thiery V., Quenardel J. M., Rossi P., 2009, Famenno-Carboniferous (370-320 Ma) strike slip tectonics monitored by syn-kinematic plutons in the French Variscan belt (Massif Armoricain and French Massif Central). Bull. Soc. Géol. Fr., 180, 3, 231-246.

Rollet N., Déverchère J., Beslier M.-O., Guennoc P., Réhault J.-P., Sosson M., Truffert C., 2002, Back arc extension, tectonic inheritance, and volcanism in the Ligurian Sea, Western Mediterranean: Ligurian Sea Back Arc structure and evolution, Tectonics, 21, 3, 6-1-6–23, doi:10.1029/2001TC900027.

Rubatto D., Schaltegger U., Lombardo B., Colombo F., Compagnoni R., 2001, Complex Paleozoic magmatic and metamorphic evolution in the Argentera Massif (Western Alps) resolved with U–Pb dating. Schweizerische mineralogische und petrographische Mitteilungen, 81, 213–228.

Sanchez G., Rolland Y., Schreiber D., Giannerini G., Corsini M., Lardeaux, J.-M., 2010, The active fault system of SW Alps. J. Geodyn., 49, 296–302.

Sanchez G., Rolland Y., Schneider J., Corsini M., Oliot E., Goncalves P., Verati C., Lardeaux J.M., Marquer D., 2011, Dating low-temperature deformation by ^{40}Ar/^{39}Ar on white mica, insights from the Argentera-Mercantour Massif (SW Alps). Lithos 125, 521 - 536.

Sarkarinejad K., Azizi A., 2008, Slip partitioning and inclined dextral transpression along the Zagros Thrust System, Iran. J Struct Geol, 30, 116-136.

Sarkarinejad K., Keshavarz S., Faghih A., 2015, Kinematics of the Sirjan mylonite nappe, Zagros Orogenic Belt: insights from strain and vorticity analyses. Journal of Geosciences, 60, 189-202.

Schneider J., Corsini M., Reverso-Peila A., Lardeaux J. M., 2014, Thermal and mechanical evolution of an orogenic wedge during Variscan collision: an example in the Maures-Tanneron massif (SE France). Geol. Soc., London, spec. publ., 405, 313-331.

Seydoux-Guillaume A.M., Paquette J.L., Wiedenbeck M., Montel J.M., Heinrich W., 2002a, Experimental resetting of the U–Th–Pb system in monazite. Chemical Geology, 191, 165–181.

Seydoux-Guillaume A.M., Wirth R., Nasdala L., Gottschalk M., Montel J.M., Heinrich W., 2002b, XRD, TEM and Raman study of experimental annealing of natural monazite. Physics and Chemistry of Minerals, 29, 240–253.

Simonetti M., Carosi R., Montomoli C., 2017, Variscan shear deformation in the Argentera Massif: a field guide to the excursion in the Pontebernardo Valley (CN, Italy). Atti della Società Toscana di Scienze Naturali Memorie, Serie A, 124, doi: 10.2424/ASTSN.M.2017.02.

Simpson C., De Paor D.G., 1993, Strain and kinematic analysis in general shear zones. Journal of Structural Geology. 15, 1-20.

Skrzypek E., Stìpskà, P., Cocherie A., 2012, The origin of zircon and the significance of U–Pb ages in high-grade metamorphic rocks: a case study from the Variscan orogenic root (Vosges Mountains, NE France). Contributions to Mineralogy and Petrology, 164, 935–957.

Stampfli G.M., von Raumer L.F., Borel G.D., 2002, Paleozoic evolution of pre-Variscan terranes: from Gondwana to the Variscan collision. Geol. S. Am. S., 364, 263-280.

Tapponnier P., Molnar P.J., 1977, Active faulting and tectonics in China. J. Geophys. Res. 82, 2905–2930.

Tapponnier P., Peltzer G., Le Dain A.Y., Armijo R., Cobbold P., 1982, Propagating extrusion tectonics in Asia: new insights from simple experiments with plasticine. Geology 10, 611–616.

Thomas J. C., Claudel M. E., Collombet M., Tricart P., Chauvin A., Dumont T., 1999, First paleomagnetic data from the sedimentary cover of the French penninic Alps: Evidence for Tertiary counterclockwise rotations in the western Alps. Earth Planet. Sci. Lett., 171, 561–574.

Thompson, A.B., Schulmann, K., Jezek, J., 1997, Thermal evolution and exhumation in obliquely convergent (transpressive) orogens. Tectonophysics, 280, 171-184.

Tiepolo M., 2003, In situ Pb geochronology of zircon with laser ablation–inductively coupled plasma-sector field mass spectrometry. Chemical Geology, 199, 159–177.

Todesco M., Vigliotti L., 1993, When did Sardinia rotate? Statistical evalutation of the paleomagnetic data. Annali di Geofisica, Vol. 30, N. 5 – 6.

Tollmann A., 1982, Großraumiger variszischer Deckenbau im Moldanubikum und neue Gedanken zum Variszikum Europas. Geotektonische Forschungen, 64, 1–91.

Turco E., Macchiavelli C., Mazzoli S., Schettino A., Pierantoni P.P., 2012, Kinematic evolution of Alpine Corsica in the framework of Mediterranean mountain belts. Tectonophysics, 579, 193-206.

Van Actherbergh E., Ryan C. G., Jackson S. E., Griffin W., 2001, Data reduction software for LA–ICP–MS. In: Sylvester, P. (Ed.), Laser Ablation ICPMS in the Earth Sciences. Mineralogical Association of Canada, Short Course Series, 29, 239 - 243.

Vigliotti L., Kent D.V., 1990, Paleomagnetic results of Tertiary sediments from Corsica: evidence of post-Eocene rotation. Phys. Earth Planet. Inter., 62, 97 - 108.

Villa I.M., Ruggieri G., Puxeddu M., 1997, Petrological and geochronological discrimination of two white-mica generations in a granite cored from the Larderello-Travale geothermal field (Italy). European Journal of Mineralogy 9, 563–568.

Villa I. M., Bucher S., Bousquet R., Kleinhanns T. C., Schmid S. M. 2014, Dating polygenic metamorphic assemblages along a transect across the the western Alps. Journal of Petrology, 55 (4), 803-830.

Villa I. M., 2015, ^{39}AR-^{40}AR geochronology of mono- and polymetamorphic basement rocks, Periodico di Mineralogia, 84 (3B), 615-632.

Vollmer f. W., 2015, EllipseFit 3 user manual, pp. 72.

von Raumer J. F., Bussy F., Schaltegger U., Schulz B., Stampfli G. M., 2013, Pre-Mesozoic Alpine basements—Their place in the European Paleozoic framework. Geol. Soc. Am. Bull., 125, 1–2, 89–108, doi:10.1130/B30654.1.

Wallis S. R., Platt J. P., Knott S. D., 1993, Recognition of syn-convergence extension in accretionary wedges with examples from Calabrian arc and the Eastern Alps. American Journal of Sciences ,293, 463-495.

Williams M. L., Jercinovic M.J., Hetherington C. J., 2007, Microprobe Monazite Geochronology: Understanding Geologic Processes by Integrating Composition and Chronology. Annual Review of Earth Planetary Sciences, 35, 137 - 75.

Wu W., Liu J., Zhang L., Qi Y., Ling C., 2016, Characterizing a middle to upper crustal shear zone: microstructures, quartz c-axis fabrics, deformation temperatures and flow vorticity analysis of the northern Ailao Shan-Red River shear zone. Journal of Asian Earth Sciences.

Xypolias P., Kokkalas S., 2006, Heterogeneous ductile deformation along a midcrustal extruding shear zone: an example from the External Hellenides (Greece). In: Law, R.D., Searle, M.P., Godin, L. (Eds.), Channel Flow, Ductile Extrusion, and Exhumation in Continental Collision Zones. Geological Society, London, Special Publications, 268, 497-516.

Xypolias P., 2010, Vorticity analysis in shear zones: A review of methods and applications. Journal of Structural Geology, 32, 2072 – 2092.

Zhang Q., Teyssier C., 2013, Flow vorticity in Zhangbaling transpressional attachment zone, SE China. Journal of Structural Geology, 48, 72-84.

Figure captions

Figure 1. A) Distribution of the Variscan units in Europe at the present day. S = Sardinia; C = Corsica; MTM = Maures-Tanneron Massif; MC = Massif Central; IM = Iberian Massif; AM = Armorican Massif; RH= Rheno-Hercynian; BM = Bohemian Massif; V = Vosges. Blue circle indicates the location of the Argentera Massif (modified

after Compagnoni et al., 2010); B) Geological sketch map of the Argentera-Mercantour Massif. FMSZ: Ferriere-Mollières shear zone; FCSZ: Fremamorta-Colle del Sabbione shear zone; BF: Bersezio fault; VLS: Valle Stura Leucogranite; ACG: Argentera Central Granite (modified after Compagnoni et al., 2010).

Figure 2. Geological map of the northwestern portion of the Ferriere-Mollières shear zone (modified after Carosi et al., 2016b). Rectangles indicate sampling areas: transect A; transect B; transect C. Details of the selected areas are shown in figure 6 and cross sections are shown in figure 14. Equal angle, lower hemisphere projections are also shown: 1) Mineral lineation (red), poles to mylonitic foliation (black) and poles to ultramylonitic foliation (yellow triangles) in mylonitic schist with biotite and white mica. 2) Mineral lineation (red) and poles to mylonitic foliation (black) in mylonitic gneiss with biotite and white mica. 3) Axial plane poles (blue) and axes (red) of the post-shearing folds. 4) Lineation (red) and mylonitic foliation poles (black) in the alpine shear zones.

Figure 3. A) protomylonites at the outcrop-scale; B) anastomosing disjunctive cleavage in protomylonites. It is possible to recognize K-feldspar, plagioclase and quartz in a medium grained biotite and sillimanite matrix with some white mica (plane-polarized light); C) mylonites at the outcrop-scale; D) disjunctive cleavage with sub-parallel cleavage domains in mylonites. Quartz, K-feldspar and plagioclase porphyroclasts in a fine grained biotite and white mica matrix are recognizable (plane-polarized light); E) ultramylonites at the outcrop-scale; F) continuous cleavage marked by white mica and chlorite in ultramylonites (plane-polarized light).

Figure 4. Micrographs (crossed polars) of the kinematic indicators showing a top-to-the-SE sense of shear in the FMSZ. The short and the long borders of each micrograph are parallel to the Z and X axes of the strain ellipsoid, respectively. A) white mica fish and S-C' fabric; B) K-feldspar σ-type porphyroclast (yellow), C' plane (green) and oblique foliation (orange) in quartz level; C) S-C' fabric. D) Subgrain rotation and recrystallization in quartz (crossed polars); E) Undulose extinction in K-feldspar porphyroclasts (crossed polars).

Figure 5. Low-angle Alpine shear zones. A) S-C fabric at the outcrop scale; B) S-C and S-C' fabric in thin section (plane-polarized light); C) Deformed foliation with biotite relicts (plane-polarized light). The short and the long borders of each micrograph are parallel to the Z and X axes of the strain ellipsoid, respectively. All kinematic indicators show a reverse top-to-the-S sense of shear.

Figure 6. Detailed geological maps of the three studied transects along which samples were collected: A) transect A; B) transect B; C) transect C. Samples used for kinematic vorticity and strain analysis are indicated with red stars, whereas samples used for the geochronological study are indicated with yellow stars. Legend as in Figure 1.

Figure 7. A) To the right, micrograph (crossed polars) showing C' planes in mylonite of the FMSZ (the short and the long borders of the micrograph are parallel to Z and X axes of the finite strain ellipsoid, respectively). To the left, schematic diagram of possible microstructures developed under general flow conditions in a mylonite with dextral sense of shear and their appearance in thin section. The flow apophyses A1 and A2 are indicated in red and green, respectively. The angle 2ν between the two apophyses (yellow) is bisected by the C' shear plane (dotted line). The equation to calculate Wk is also shown (modified after Kurz and Northrup, 2008). B) Relation to calculate the shortening value S perpendicular to the flow plane on the basis of the values of both the mean kinematic vorticity number Wm, that can be assumed equal to Wk, and the axial ratio of the strain ellipse measured on the XZ section (modified after Law et al., 2004).

Figure 8. Polar histograms used to derive the angle ν and to calculate kinematic vorticity with the S-C' method (Kurz and Northrup, 2008) on field oriented samples. A1 = flow apophysis 1; A2 = flow apophysis 2. Dashed line represent the bisector of the angle between A1 and A2, green bars represent the number of data. All histograms are shown with the same sense of shear (red arrows).

Figure 9. Fry graphs used in the strain analysis obtained with the center-to-center method on the XZ sections; n = number of centers used for the Fry analysis. A) ARG 143; B) ARG 144; C) ARG 21a; D) ARG 68; E) ARG 117; F) ARG 19; G) ARG 21; H) ARG 27; I) ARG 29. Axial ratios Rxz are reported in table 1.

Figure 10. Back-scattered electron pictures of monazite grains in different microstructural position: A) Mnz 59, sample ARG 48b, included in garnet; B) Mnz 29, sample ARG 29, included in a white mica fish; C) Monazite with asymmetric

shape along the main foliation marked by biotite in protomylonte (Mnz 14, sample ARG19); D) Monazite along the main foliation in mylonite (Mnz 52, sample ARG 27).

Figure 11. Back-scattered electron images of the analyzed monazites and related compositional maps of Y made by electron microprobe. Red dots represent the spots of the quantitative chemical analyses (data are reported in Online Resource 1).

Figure 12. Distribution of $^{206}Pb/^{238}U$ (A) and $^{208}Pb/^{232}Th$ (B) ages for different samples along the deformation gradient. Black vertical bars indicate concordant ages, black horizontal bar contains the averaged data (MSWD=Mean Square Weighted Deviates; prob.= probability). Geochronological data define a broad trend (grey area) reflecting the deformation degree.

Figure 13. A) Percentage of pure shear (PS) and simple shear (SS) in relation to the calculated maximum and minimum Wk values; B) simplified sketch showing orientation of the instantaneous flow elements and their angular relationships in a dextral shear zone with simultaneous pure shear and simple shear, θ is the angle between ISA_{max} and the shear zone boundary (modified after Xypolias, 2010); C) diagram showing relationship between the orientation of the maximum Istantaneous Stretching Axis (ISA_{max}) with respect to the shear zone boundary (angle θ) related to the kinematic vorticity number Wk (modified after Fossen and Tikoff, 1993; Fossen et al., 1994) Wk value for which simple shear = pure shear is 0,71 according to Law et al., 2004 and Xypolias, 2010. The distribution of the samples shows a variation from a pure shear dominated transpression to a simple shear dominated transpression linked to the increase of the vorticity number. Orange dashed line represents the theoretical trend of the angle θ. It is possible to observe that the distribution of the values of angle θ of the studied samples is in good agreement with the theoretical curve; D) variation of the vorticity number in relation with the distance of the sample from the center of the shear zone. The distribution of points shows increasing Wk values (i.e. increasing of simple shear component of deformation) toward the central part of the shear zone (trend: blue dashed line).

Figure 14. Parallel cross sections along the deformation gradient (modified after Carosi et al., 2016b). The position of the analyzed samples and the relative $^{206}Pb/^{238}U$ (red) and $^{208}Pb/^{232}Th$ (blue) ages are reported. Traces of the geological cross sections and the legend are reported in figure 2.

Figure 15. Evolution of the Ferriere-Molliéres Shear Zone according to a type II growth model (Fossen, 2010) and relationship between deformation gradient and age of shear deformation: the margins become progressively inactive and preserve the features acquired during the older stages of shearing while the active part gets progressively thinner and records the younger stages of shear zone activity.

Figure 16. Reconstruction of the Variscan Belt during Permian (modified after Guillot and Ménot, 2009; Carosi et al., 2012). Age of shearing in the eastern sector of the Variscan Belt are reported. The East Variscan Shear Zone (EVSZ) affects the Argentera-Mercantour Massif (AR) at ~ 340 Ma and then propagated southward affecting the Maures-Tanneron Massif (MTM) and Corsica and Sardinia (SA) at ~ 320 Ma (Carosi et al., 2012). BM = Bohemian Massif.

Table 1. Kinematic vorticity numbers obtained by the S-C' method and strain data of samples from the three transects. N = number of C' plane; ν *max* = mesured maximum angle between C' plane and S plane; 2ν = calculated angle between apophysis A1 and apophysis A2; Wk = vorticity number; Angle θ = angle between the ISA_{max} and the shear zone boundary; n = number of centers used for the Fry analysis. Shortening and Stretching values, deformation and position of the sample are also reported.

Table 2. Standards analyzed for the geochronological study at the beginning and at the end of each run.

Table 3. Geochronological data obtained from the monazites of the samples ARG 19, ARG 21, ARG 27, ARG 29 and ARG 48b.

Online Resource 1. Chemical quantitative analyses of the monazites of the sample ARG 19, ARG 21, ARG 27, ARG 29 and ARG 48b.

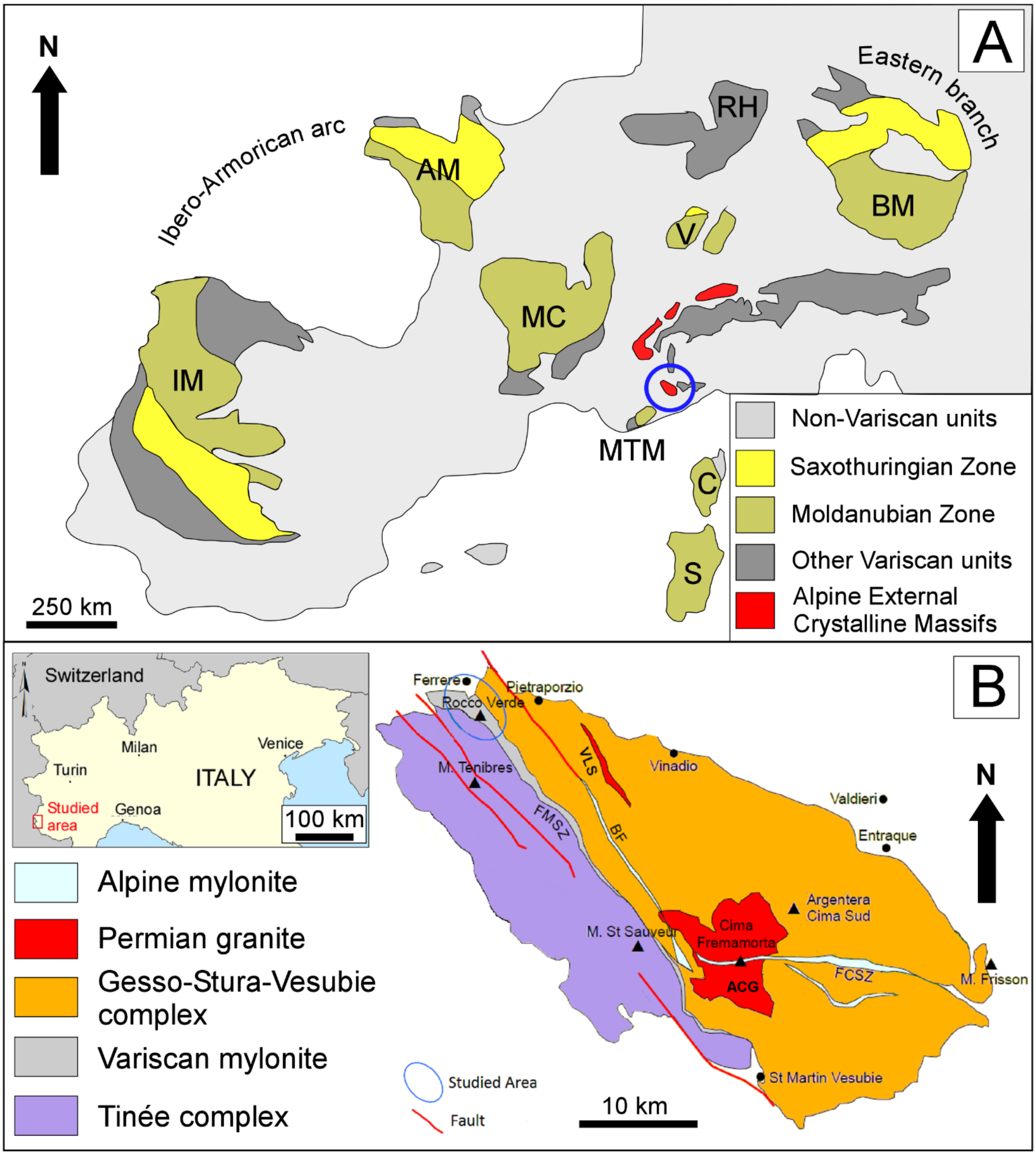
A
N
Ibero-Armorican arc
Eastern branch
AM
RH
BM
V
MC
IM
MTM
C
S
250 km
Non-Variscan units
Saxothuringian Zone
Moldanubian Zone
Other Variscan units
Alpine External
Crystalline Massifs
B
Switzerland
Milan
Venice
Turin
ITALY
Studied
area
Genoa
100 km
Alpine mylonite
Permian granite
Gesso-Stura-Vesubie
complex
Variscan mylonite
Tinée complex
Ferrere
Pietraporzio
Rocco Verde
M. Tenibres
VLS
Vinadio
FMSZ
BF
Valdieri
Entraque
N
Argentera
Cima Sud
M. St Sauveur
Cima
Fremamorta
ACG
FCSZ
M. Frisson
St Martin Vesubie
Studied Area
Fault
10 km

Fig.1

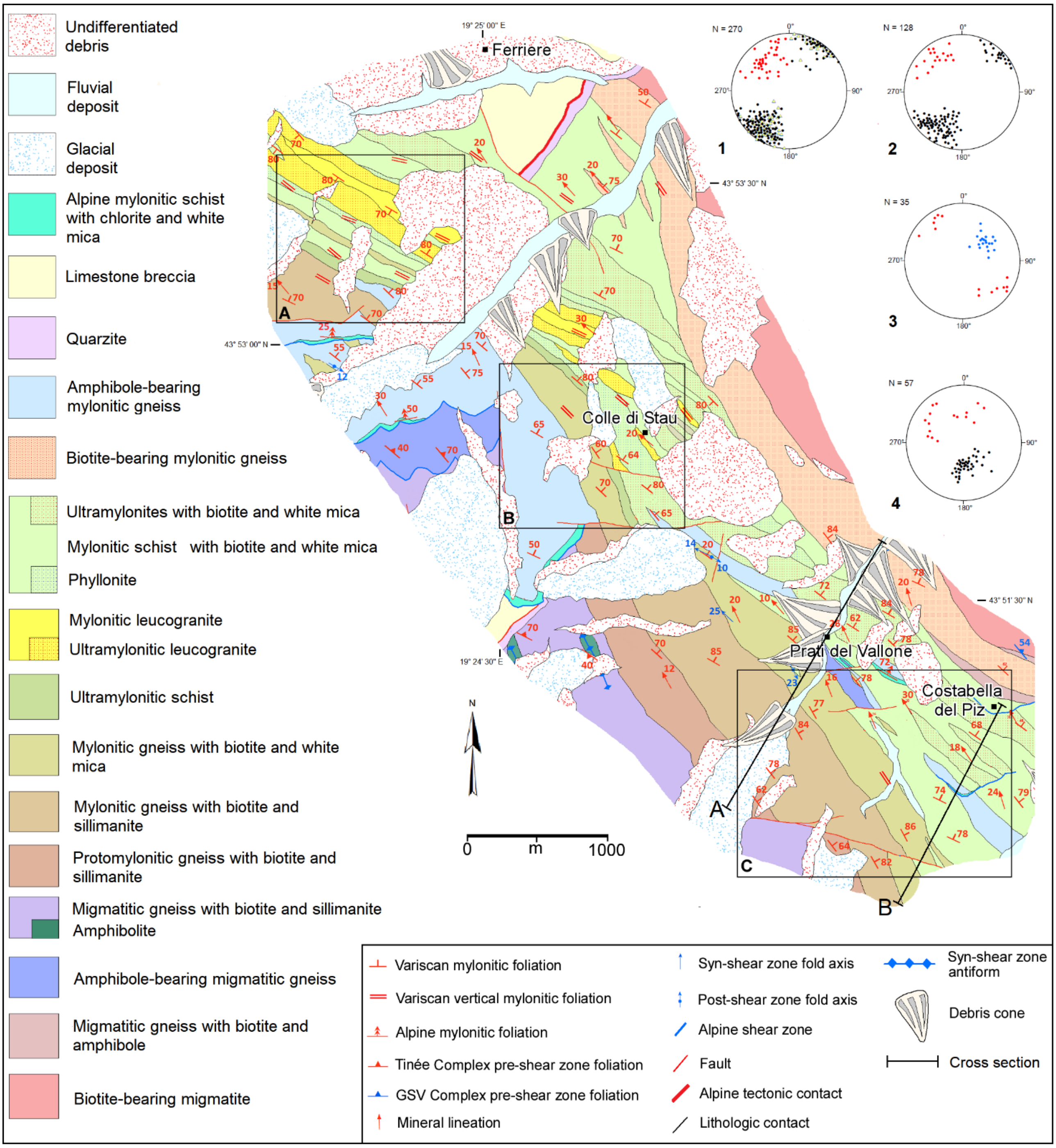
Undifferentiated debris
Fluvial deposit
Glacial deposit
Alpine mylonitic schist with chlorite and white mica
Limestone breccia
Quarzite
Amphibole-bearing mylonitic gneiss
Biotite-bearing mylonitic gneiss
Ultramylonites with biotite and white mica
Mylonitic schist with biotite and white mica
Phyllonite
Mylonitic leucogranite
Ultramylonitic leucogranite
Ultramylonitic schist
Mylonitic gneiss with biotite and white mica
Mylonitic gneiss with biotite and sillimanite
Protomylonitic gneiss with biotite and sillimanite
Migmatitic gneiss with biotite and sillimanite
Amphibolite
Amphibole-bearing migmatitic gneiss
Migmatitic gneiss with biotite and amphibole
Biotite-bearing migmatite
Variscan mylonitic foliation
Variscan vertical mylonitic foliation
Alpine mylonitic foliation
Tinée Complex pre-shear zone foliation
GSV Complex pre-shear zone foliation
Mineral lineation
Syn-shear zone fold axis
Post-shear zone fold axis
Alpine shear zone
Fault
Alpine tectonic contact
Lithologic contact
Syn-shear zone antiform
Debris cone
Cross section
Ferriere
Colle di Stau
Prati del Vallone
Costabella del Piz
19° 25' 00" E
19° 24' 30" E
43° 53' 30" N
43° 53' 00" N
43° 51' 30" N
N
0
m
1000
N = 270
N = 128
N = 35
N = 57

Fig.2

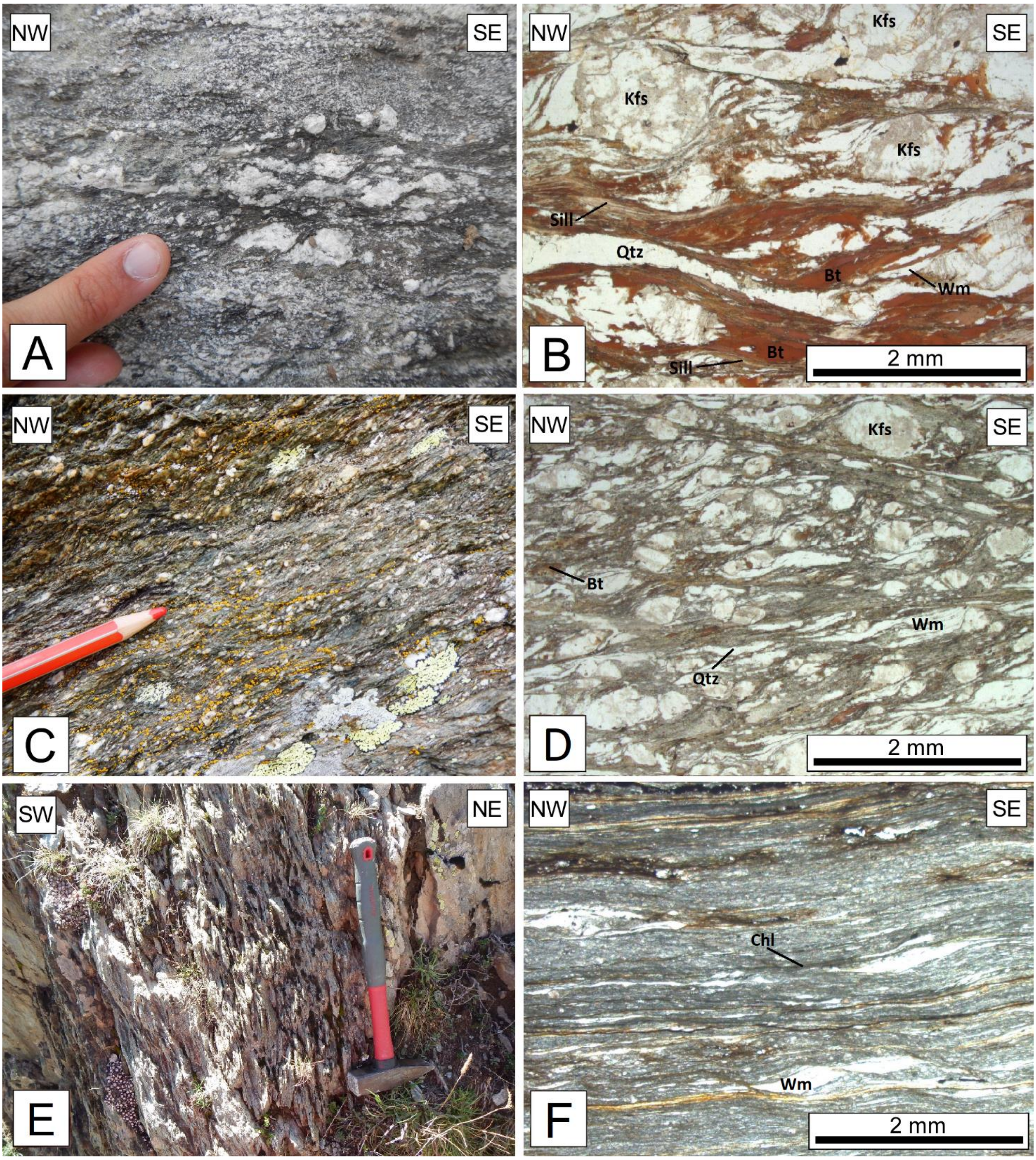
NW
SE
A
NW
Kfs
SE
Kfs
Kfs
Sill
Qtz
Bt
Wm
B
Bt
Sill
2 mm
NW
SE
C
NW
Kfs
SE
Bt
Wm
Qtz
D
2 mm
SW
NE
E
NW
SE
Chl
Wm
F
2 mm

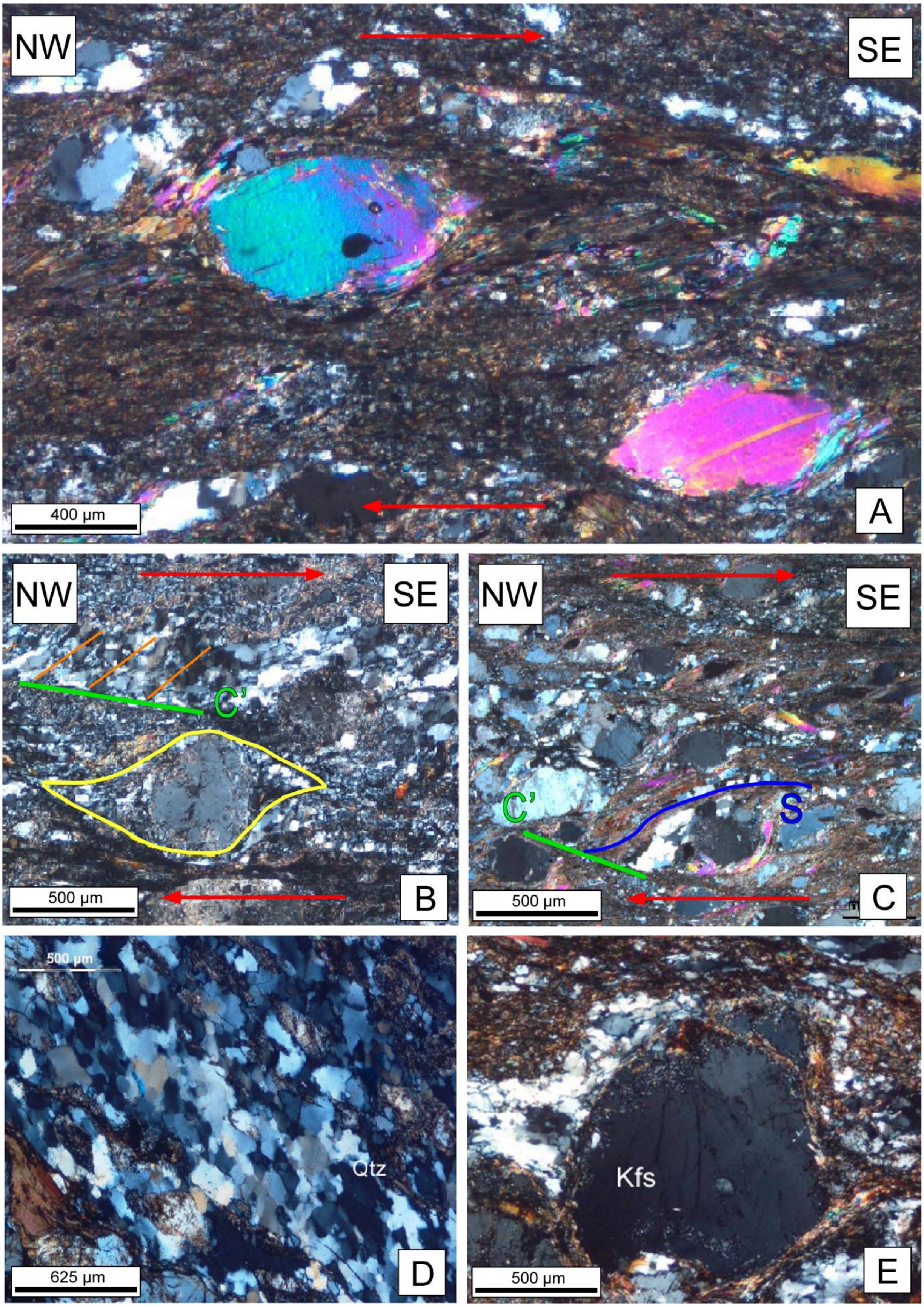
NW
SE
400 µm
A
NW
SE
C'
500 µm
B
NW
SE
C'
S
500 µm
C
500 µm
Qtz
625 µm
D
Kfs
500 µm
E

923

924 Fig.4

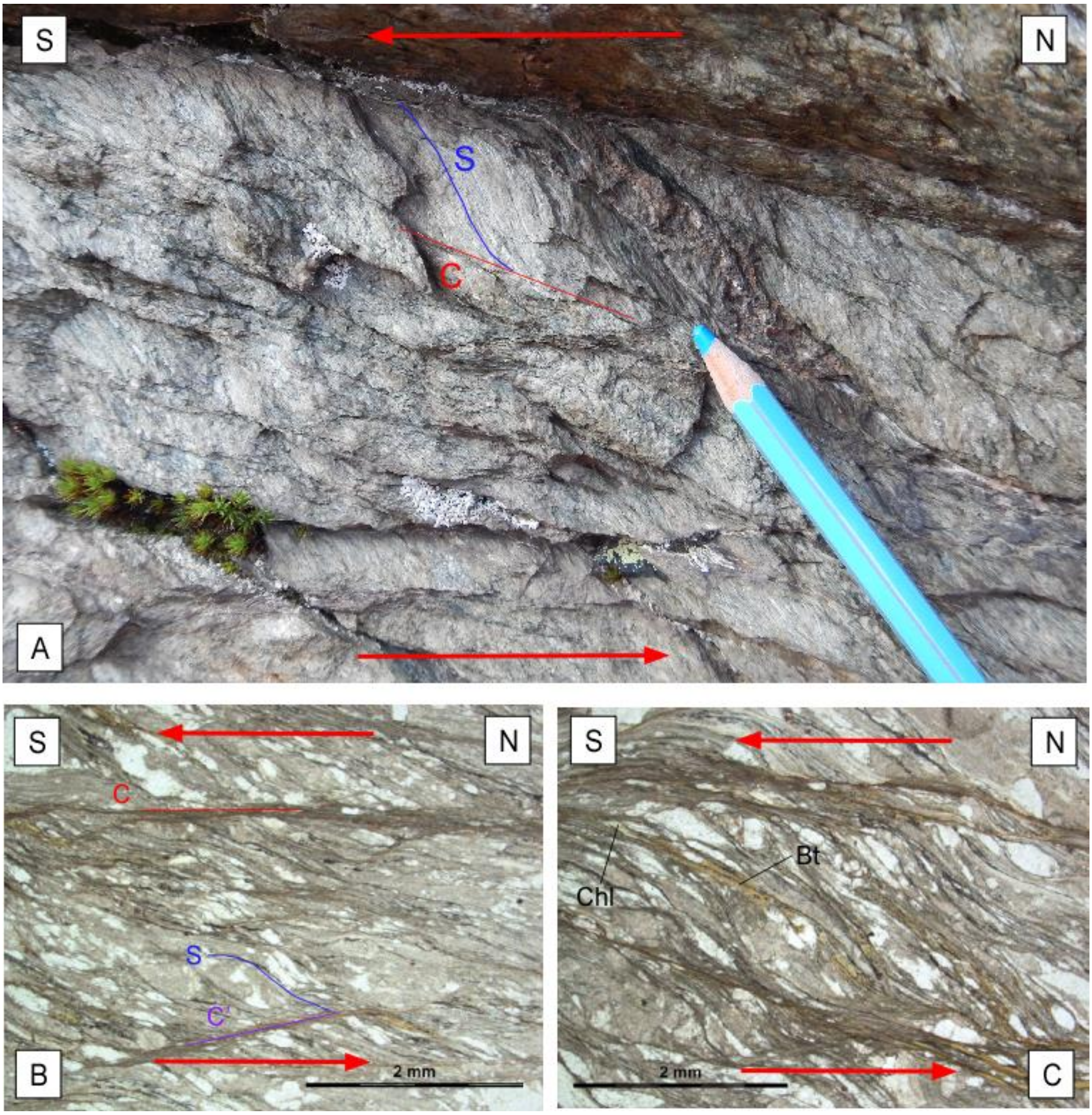

Fig.5

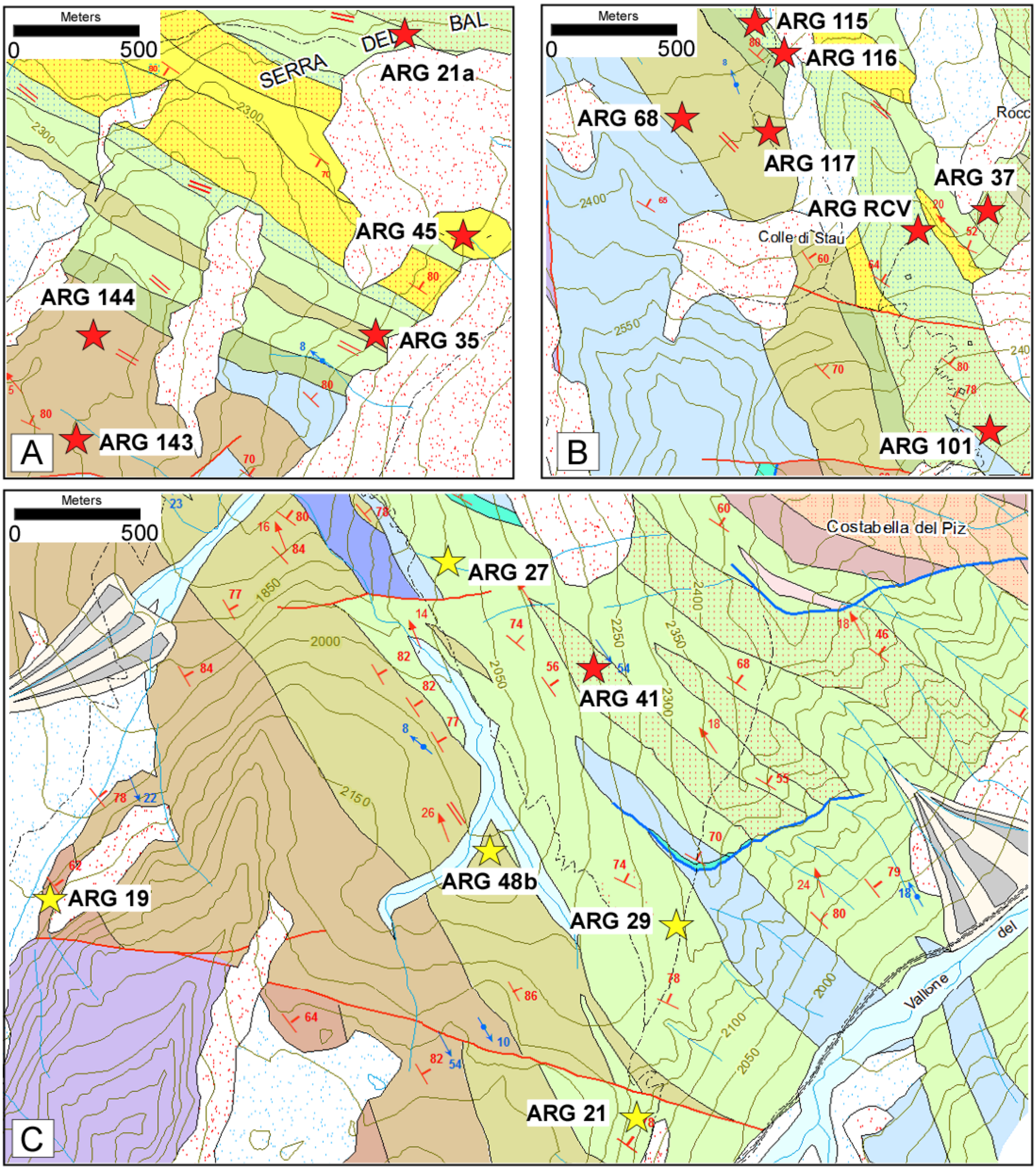
Meters
0
500
SERRA
DEL
BAL
ARG 21a
ARG 45
ARG 144
ARG 35
ARG 143
A
Meters
0
500
ARG 115
ARG 116
ARG 68
ARG 117
ARG 37
ARG RCV
Colle di Stau
ARG 101
B
Meters
0
500
ARG 27
Costabella del Piz
ARG 41
ARG 48b
ARG 19
ARG 29
Vallone
del
ARG 21
C

Fig.6

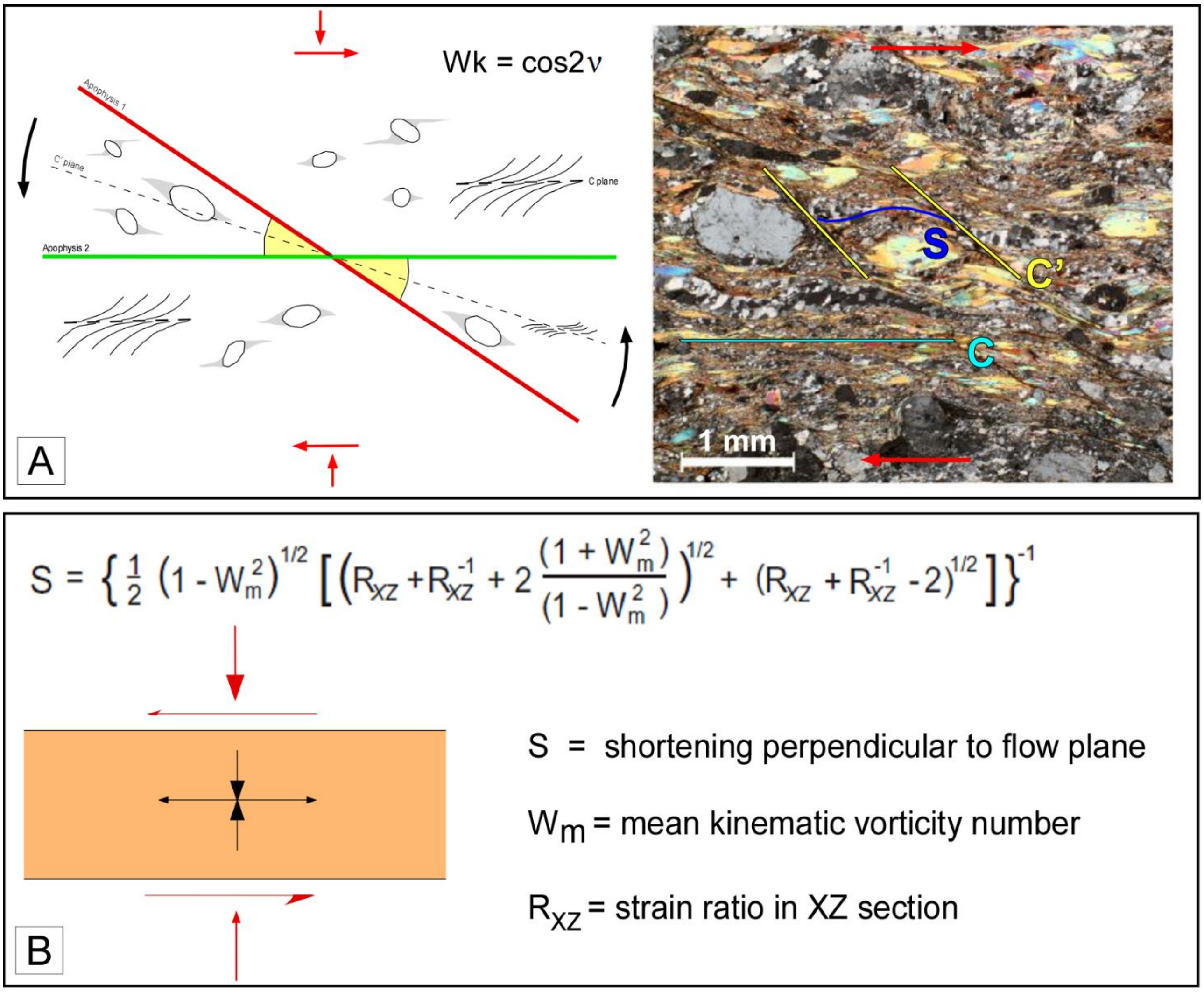
Wk = cos2ν
Apophysis 1
C' plane
C plane
Apophysis 2
A
S
C'
C
1 mm
$S = \left\{ \frac{1}{2} (1 - W_m^2)^{1/2} \left[\left(R_{XZ} + R_{XZ}^{-1} + 2 \frac{(1 + W_m^2)}{(1 - W_m^2)} \right)^{1/2} + (R_{XZ} + R_{XZ}^{-1} - 2)^{1/2} \right] \right\}^{-1}$
S = shortening perpendicular to flow plane
W_m = mean kinematic vorticity number
R_{XZ} = strain ratio in XZ section
B

Fig.7

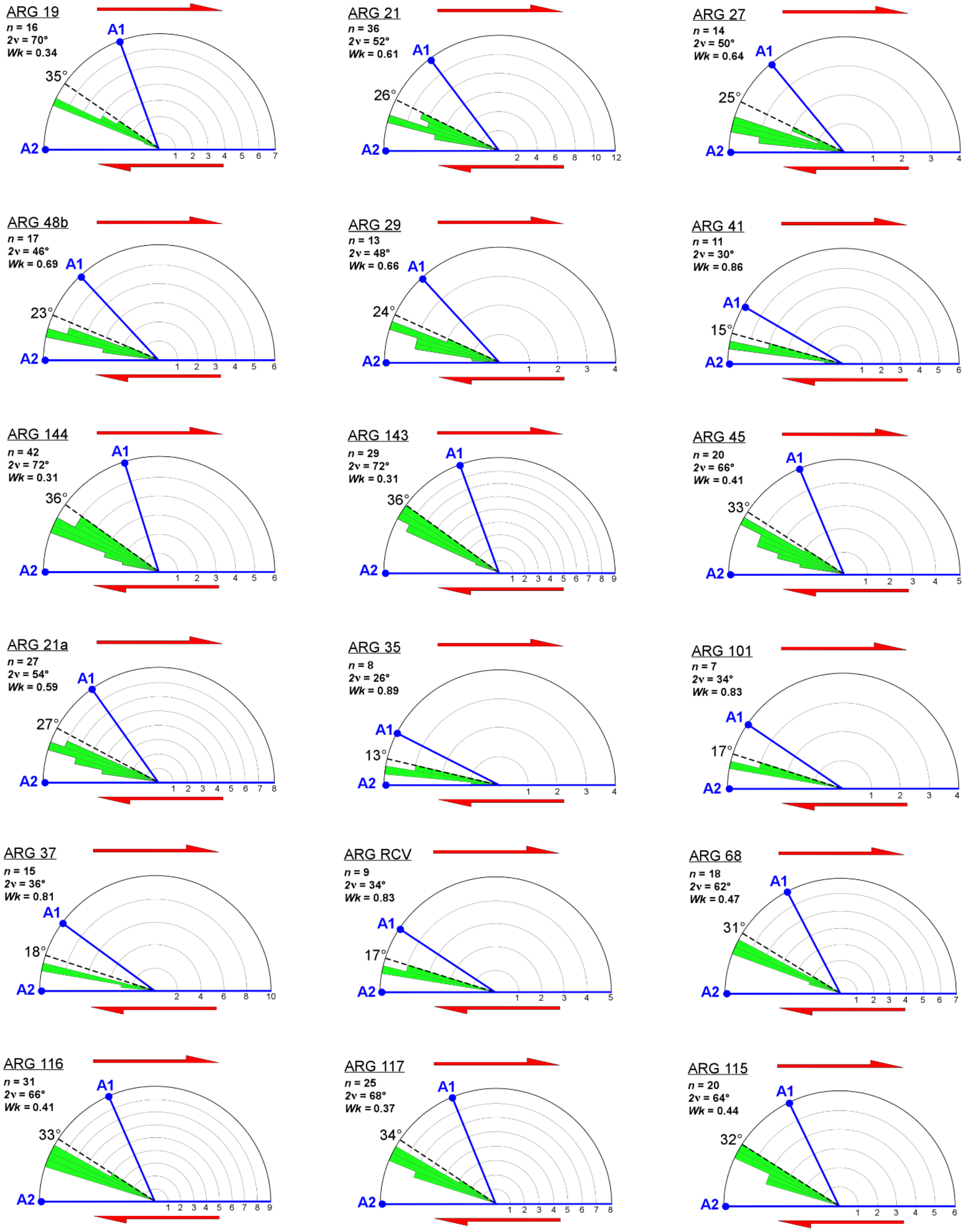
ARG 19
n = 16
2v = 70°
Wk = 0.34
35°
ARG 21
n = 36
2v = 52°
Wk = 0.61
26°
ARG 27
n = 14
2v = 50°
Wk = 0.64
25°
ARG 48b
n = 17
2v = 46°
Wk = 0.69
23°
ARG 29
n = 13
2v = 48°
Wk = 0.66
24°
ARG 41
n = 11
2v = 30°
Wk = 0.86
15°
ARG 144
n = 42
2v = 72°
Wk = 0.31
36°
ARG 143
n = 29
2v = 72°
Wk = 0.31
36°
ARG 45
n = 20
2v = 66°
Wk = 0.41
33°
ARG 21a
n = 27
2v = 54°
Wk = 0.59
27°
ARG 35
n = 8
2v = 26°
Wk = 0.89
13°
ARG 101
n = 7
2v = 34°
Wk = 0.83
17°
ARG 37
n = 15
2v = 36°
Wk = 0.81
18°
ARG RCV
n = 9
2v = 34°
Wk = 0.83
17°
ARG 68
n = 18
2v = 62°
Wk = 0.47
31°
ARG 116
n = 31
2v = 66°
Wk = 0.41
33°
ARG 117
n = 25
2v = 68°
Wk = 0.37
34°
ARG 115
n = 20
2v = 64°
Wk = 0.44
32°
A1
A2

Fig.8

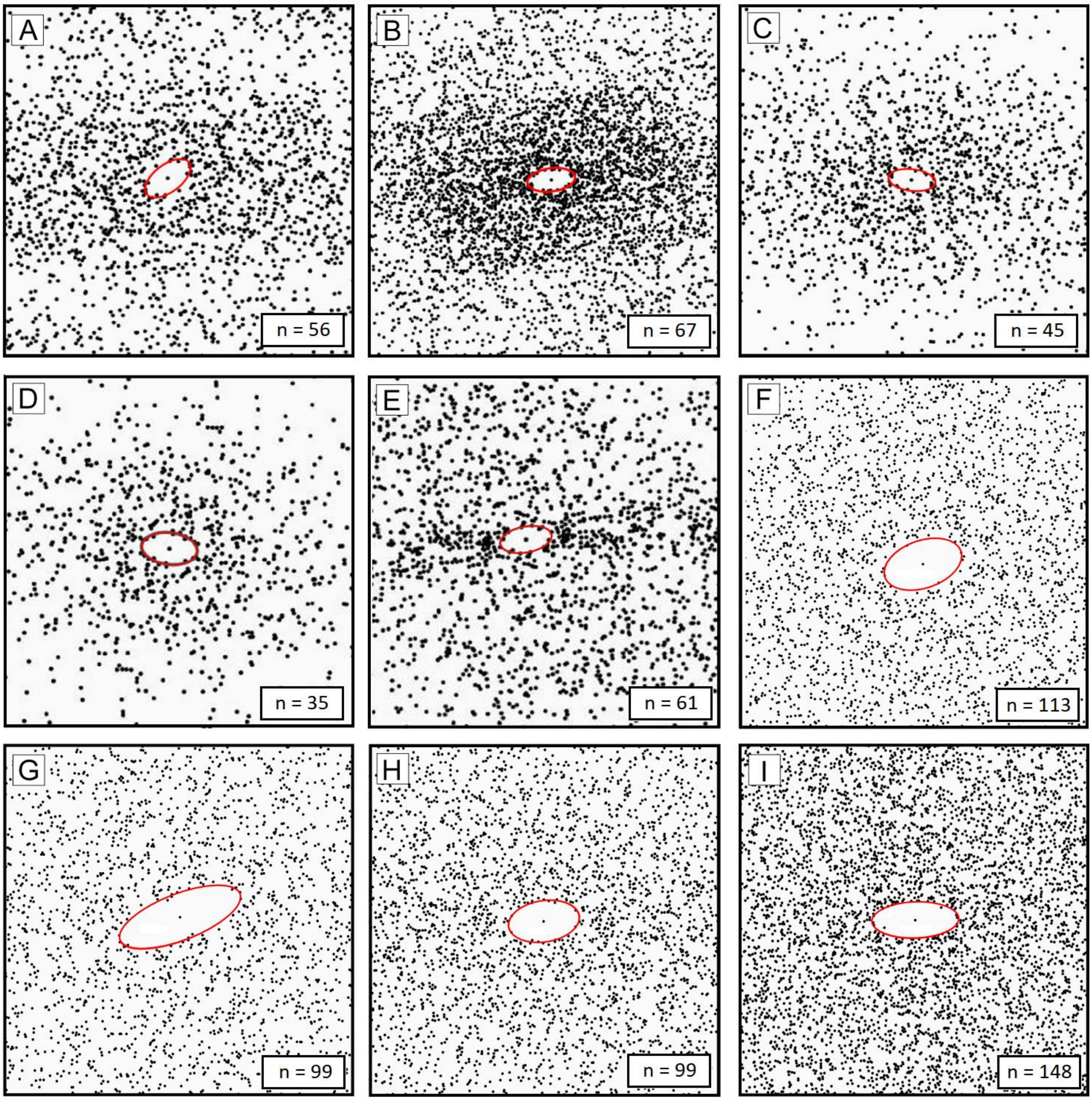

Fig.9

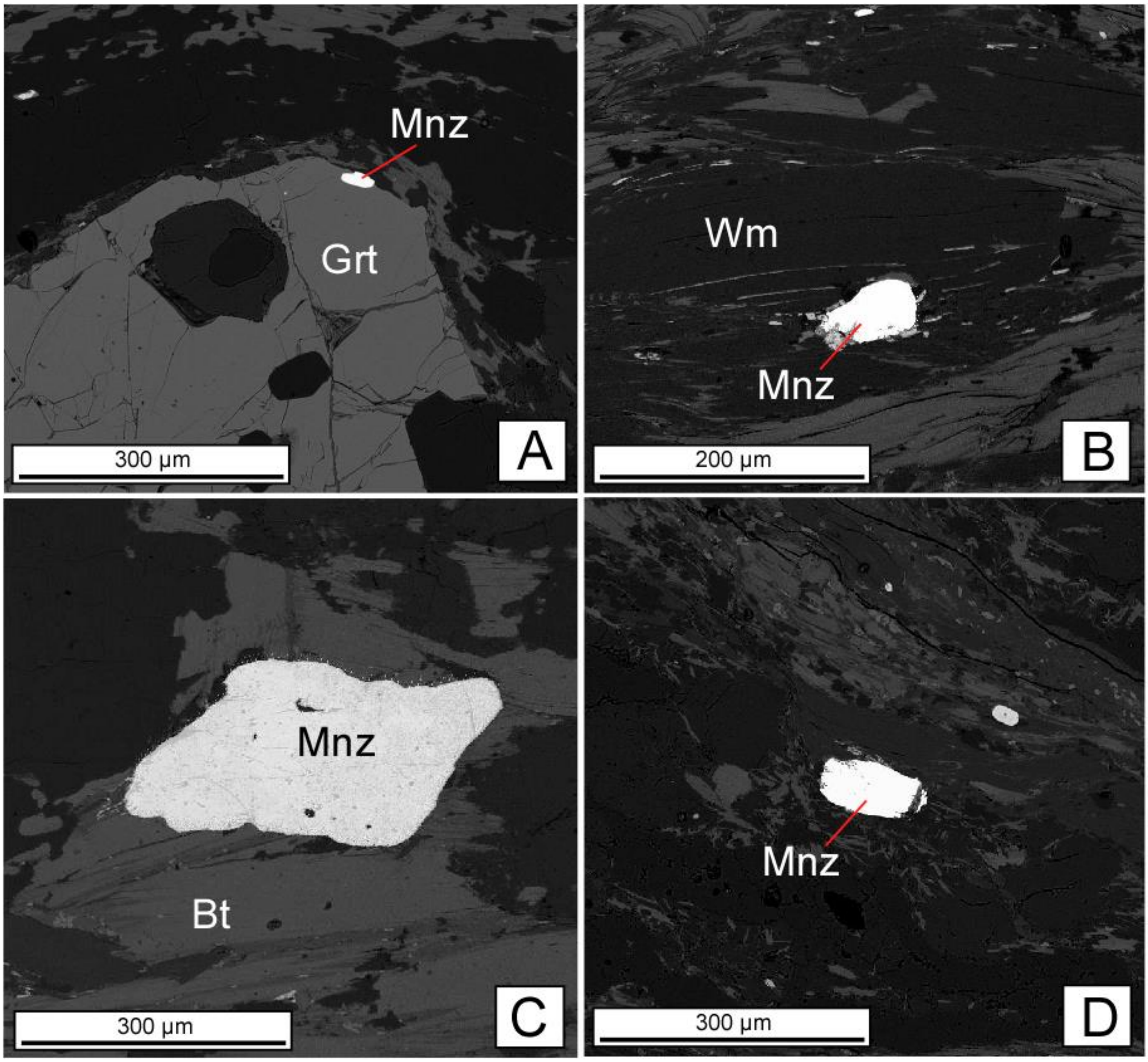

Fig.10

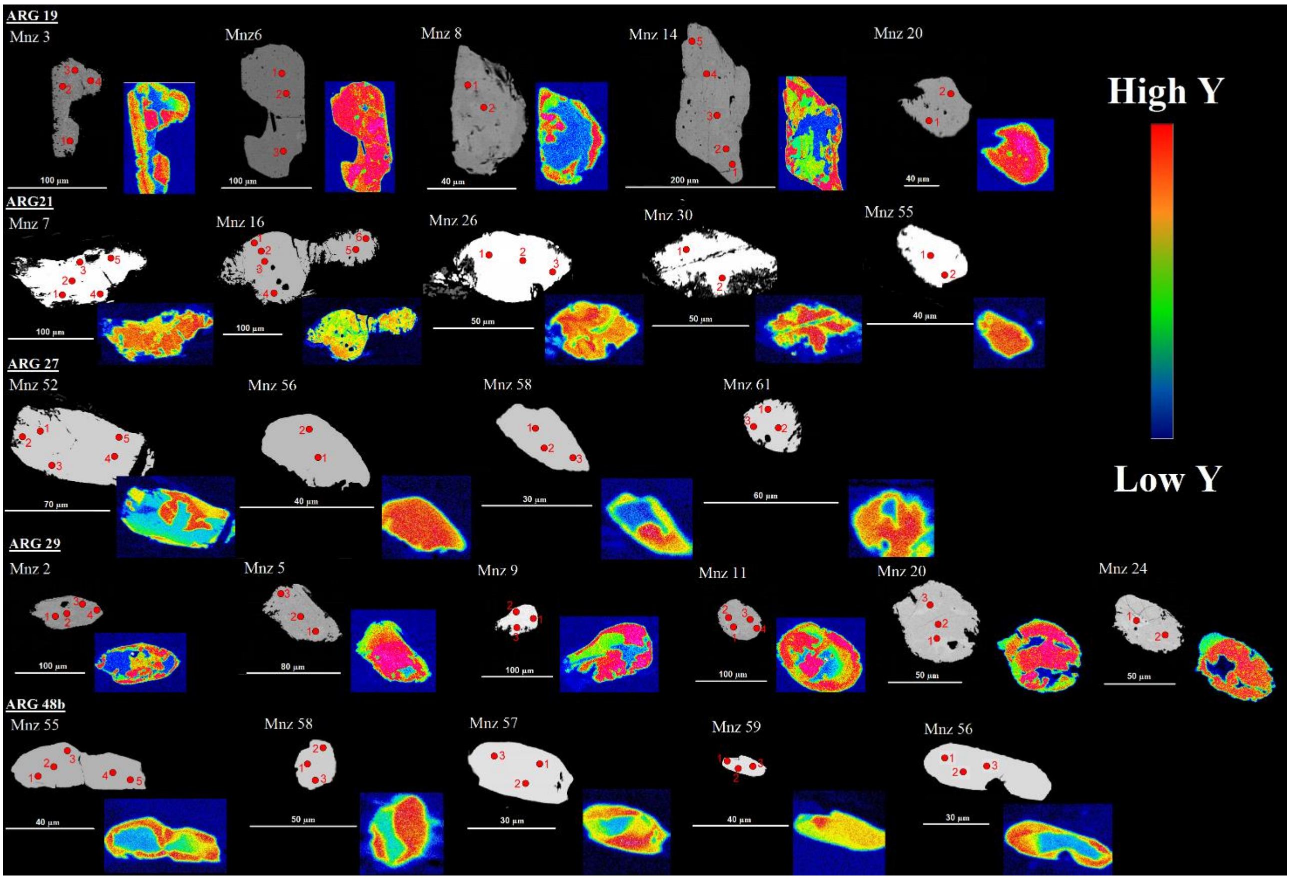
ARG 19
Mnz 3
Mnz6
Mnz 8
Mnz 14
Mnz 20
High Y
Low Y
ARG21
Mnz 7
Mnz 16
Mnz 26
Mnz 30
Mnz 55
ARG 27
Mnz 52
Mnz 56
Mnz 58
Mnz 61
ARG 29
Mnz 2
Mnz 5
Mnz 9
Mnz 11
Mnz 20
Mnz 24
ARG 48b
Mnz 55
Mnz 58
Mnz 57
Mnz 59
Mnz 56

Fig.11

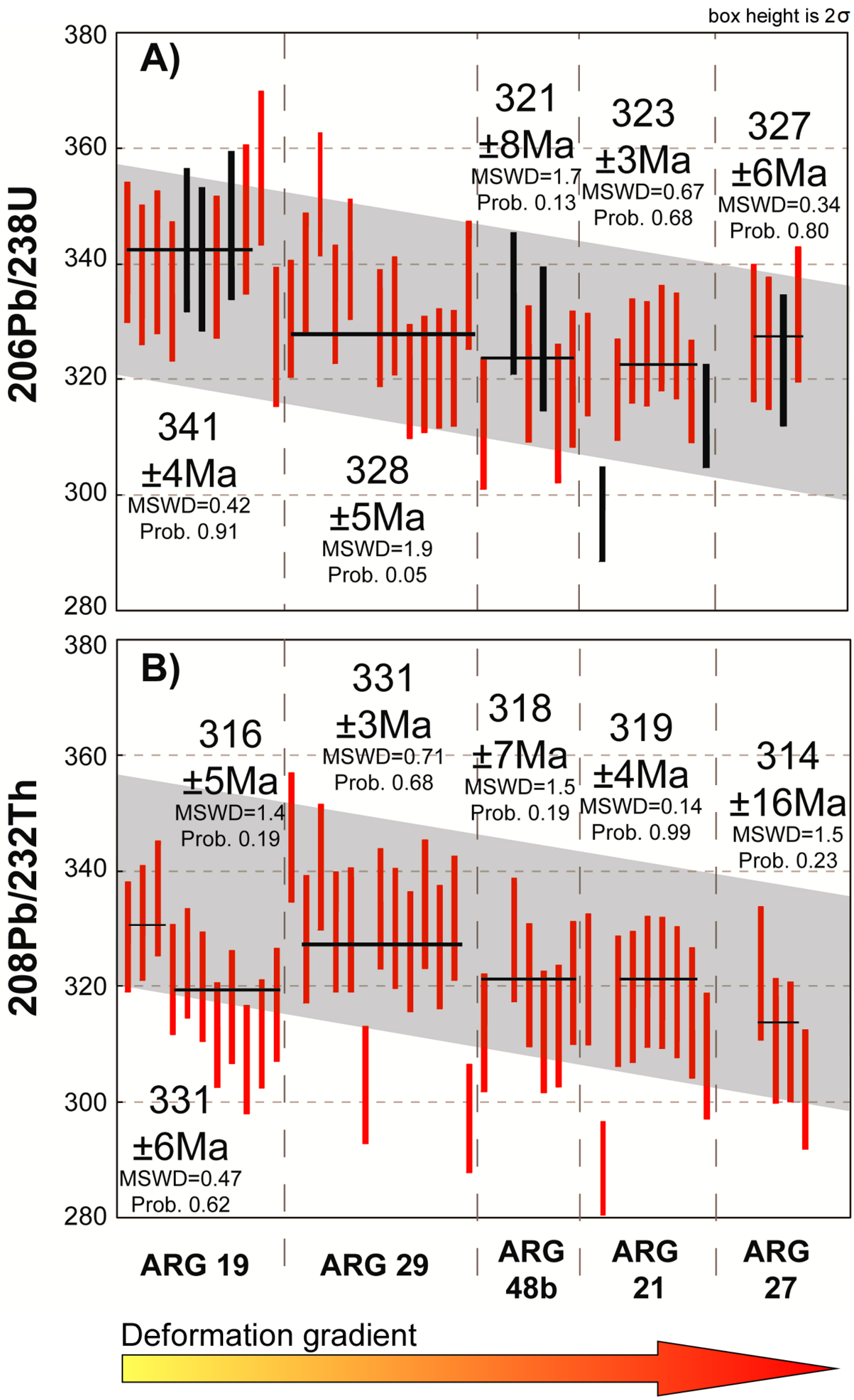
box height is 2σ
A)
206Pb/238U
380
360
340
320
300
280
321
±8Ma
MSWD=1.7
Prob. 0.13
323
±3Ma
MSWD=0.67
Prob. 0.68
327
±6Ma
MSWD=0.34
Prob. 0.80
341
±4Ma
MSWD=0.42
Prob. 0.91
328
±5Ma
MSWD=1.9
Prob. 0.05
B)
208Pb/232Th
316
±5Ma
MSWD=1.4
Prob. 0.19
331
±3Ma
MSWD=0.71
Prob. 0.68
318
±7Ma
MSWD=1.5
Prob. 0.19
319
±4Ma
MSWD=0.14
Prob. 0.99
314
±16Ma
MSWD=1.5
Prob. 0.23
331
±6Ma
MSWD=0.47
Prob. 0.62
ARG 19
ARG 29
ARG 48b
ARG 21
ARG 27
Deformation gradient

Fig.12

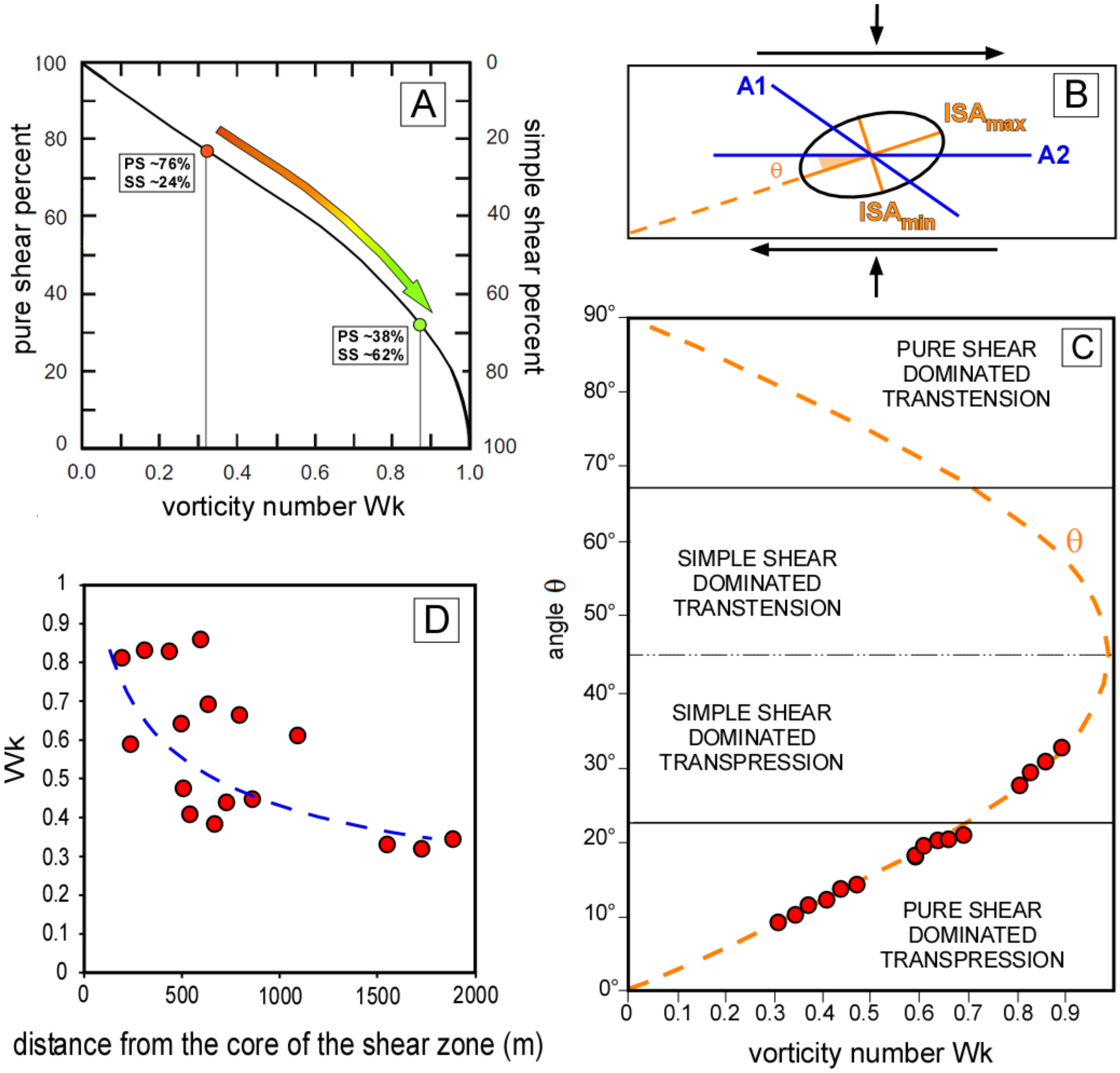
A
PS ~76%
SS ~24%
PS ~38%
SS ~62%
pure shear percent
simple shear percent
vorticity number Wk
B
A1
A2
ISAmax
ISAmin
θ
C
PURE SHEAR DOMINATED TRANSTENSION
SIMPLE SHEAR DOMINATED TRANSTENSION
SIMPLE SHEAR DOMINATED TRANSPRESSION
PURE SHEAR DOMINATED TRANSPRESSION
angle θ
vorticity number Wk
D
Wk
distance from the core of the shear zone (m)

Fig.13

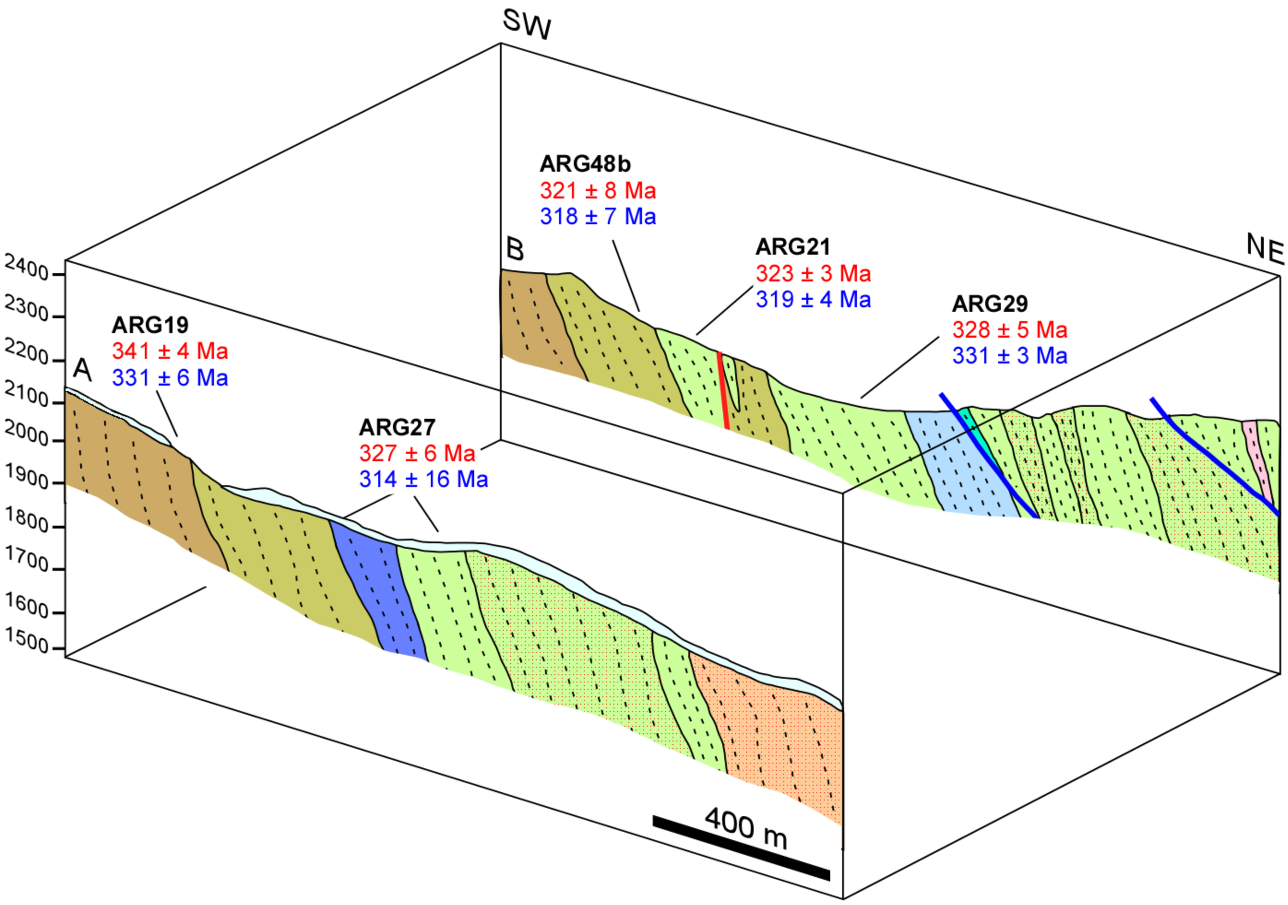
SW
NE
A
B
2400
2300
2200
2100
2000
1900
1800
1700
1600
1500
ARG19
341 ± 4 Ma
331 ± 6 Ma
ARG27
327 ± 6 Ma
314 ± 16 Ma
ARG48b
321 ± 8 Ma
318 ± 7 Ma
ARG21
323 ± 3 Ma
319 ± 4 Ma
ARG29
328 ± 5 Ma
331 ± 3 Ma
400 m

Fig.14

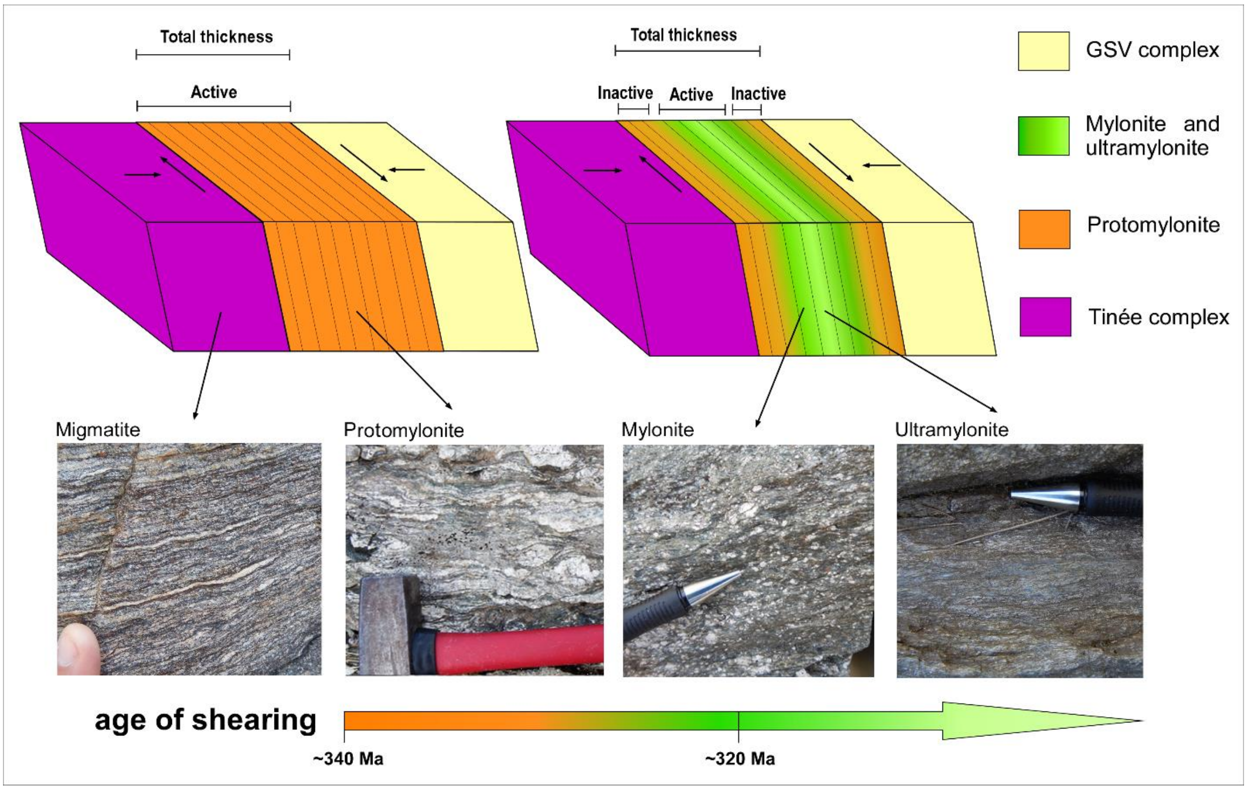
Total thickness
Active
Total thickness
Inactive
Active
Inactive
GSV complex
Mylonite and ultramylonite
Protomylonite
Tinée complex
Migmatite
Protomylonite
Mylonite
Ultramylonite
age of shearing
~340 Ma
~320 Ma

Fig.15

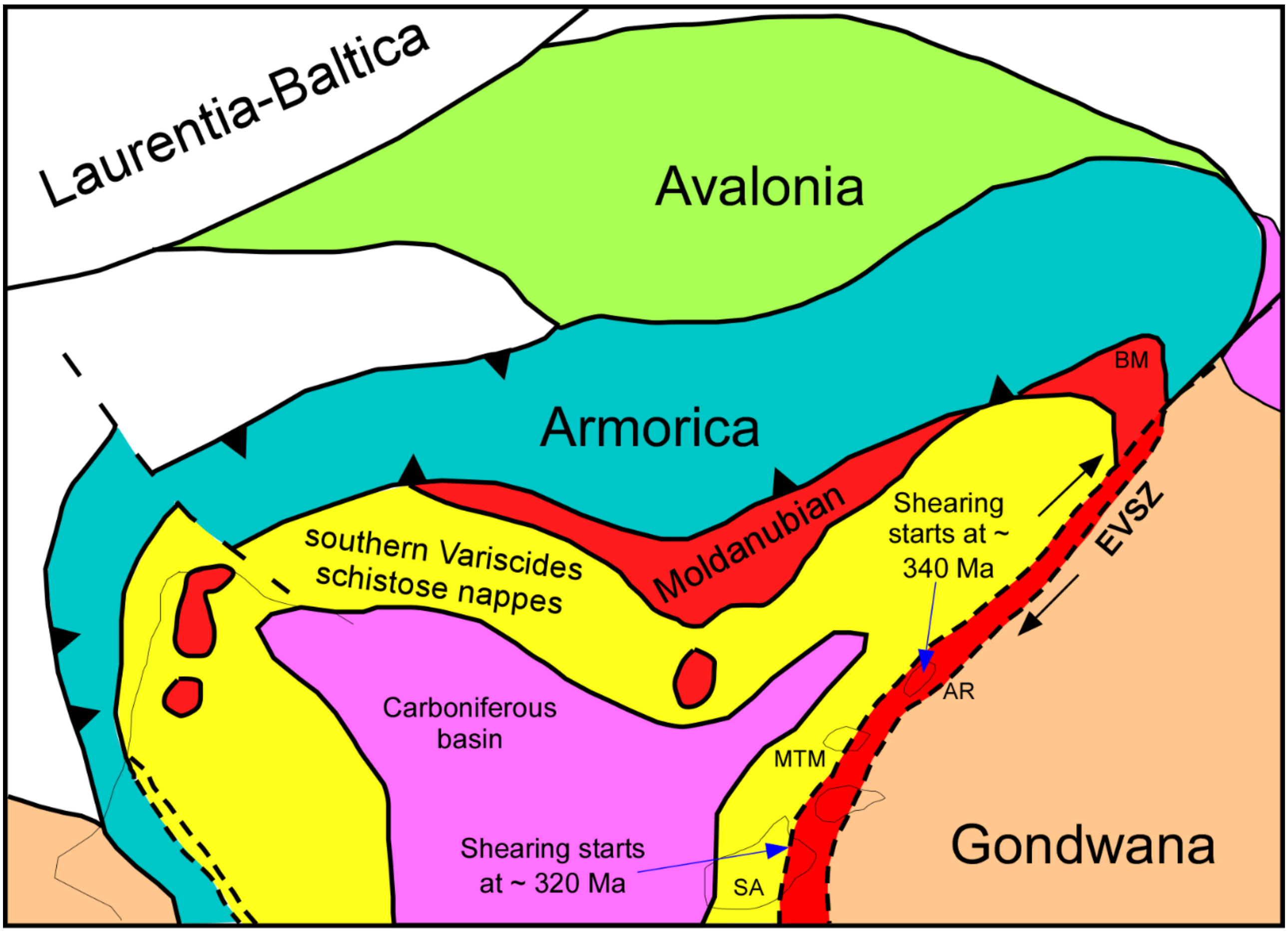

Fig.16

SAMPLE	N	v *max*	2v	Wk	Angle θ	n	Rxz	Shortening (S)	Stretching (1/S)	Deformation	Transect
ARG 144	42	36°	72°	0,31	9°	67	1,88	0,74	1,35	Protomylonite	A
ARG 143	29	36°	72°	0,31	9°	56	1,99	0,72	1,38	Protomylonite	A
ARG45	20	33°	66°	0,41	12°	-	-	-	-	Mylonite	A
ARG 21a	27	27°	54°	0,59	18°	45	2,1	0,74	1,35	Mylonite	A
ARG 35	8	13°	26°	0,89	31°	-	-	-	-	Ultramylonite	A
ARG 101	7	17°	34°	0,83	28°	-	-	-	-	Ultramylonite	B
ARG 37	15	18°	36°	0,81	27°	-	-	-	-	Ultramylonite	B
ARG RCV	9	17°	34°	0,83	28°	-	-	-	-	Ultramylonite	B
ARG 68	18	31°	62°	0,47	14°	35	1,87	0,76	1,31	Mylonite	B
ARG 116	31	33°	66°	0,41	12°	-	-	-	-	Mylonite	B
ARG 117	25	34°	68°	0,37	11°	61	2,05	0,71	1,39	Mylonite	B
ARG 115	20	32°	64°	0,44	13°	-	-	-	-	Mylonite	B
ARG 19	16	35°	70°	0,34	10°	113	1,71	0,78	1,28	Protomylonite	C
ARG 21	36	26°	52°	0,61	19°	99	2,85	0,63	1,59	Mylonite	C
ARG 27	14	25°	50°	0,64	20°	99	1,75	0,81	1,23	Mylonite	C
ARG 48B	17	23°	46°	0,69	21°	-	-	-	-	Mylonite	C
ARG 29	13	24°	48°	0,66	20°	148	2,46	0,72	1,38	Mylonite	C
ARG 41	11	15°	30°	0,86	30°	-	-	-	-	Ultramylonite	C

Tab.1

			$^{207}Pb/^{206}Pb$			$^{207}Pb/^{235}U$			$^{206}Pb/^{238}U$			$^{208}Pb/^{232}Th$			Ages							
Identifier	Comments		Ratio	1s %	1s % (Prop	Ratio	1s %	1s % (Prop	Ratio	1s %	1s % (Prop	Ratio	1s %	1s % (Prop	$^{207}Pb/^{206}Pb$	1s abs	$^{207}Pb/^{235}U$	1s abs	$^{206}Pb/^{238}U$	1s abs	$^{208}Pb/^{232}Th$	1s abs
Ju08a001	begin		0,05630	0,06%	0,10%	0,64227	0,77%	1,14%	0,08274	0,10%	0,11%	0,02538	0,04%	0,04%	464	8	504	9	512	7	507	9
Ju08a003	begin		0,05708	0,06%	0,10%	0,65076	0,80%	1,18%	0,08270	0,11%	0,11%	0,02535	0,04%	0,04%	495	9	509	9	512	7	506	9
Ju08a004	begin		0,05629	0,06%	0,10%	0,63652	0,78%	1,15%	0,08203	0,10%	0,11%	0,02501	0,04%	0,04%	464	8	500	9	508	7	499	9
Ju08a015	end		0,05790	0,06%	0,10%	0,65608	0,86%	1,22%	0,08220	0,11%	0,12%	0,02522	0,04%	0,04%	526	9	512	10	509	7	503	9
Ju08a016	end		0,05609	0,06%	0,10%	0,64304	0,85%	1,20%	0,08316	0,11%	0,12%	0,02493	0,04%	0,04%	456	8	504	9	515	7	498	9
Ju08a017	end		0,05580	0,06%	0,10%	0,63342	0,84%	1,19%	0,08234	0,11%	0,12%	0,02561	0,04%	0,04%	444	8	498	9	510	7	511	9
Ju08b001	begin		0,05758	0,06%	0,14%	0,65908	0,87%	1,60%	0,08304	0,11%	0,14%	0,02527	0,04%	0,04%	514	12	514	12	514	9	504	9
Ju08b002	begin		0,05519	0,06%	0,13%	0,63537	0,85%	1,54%	0,08352	0,11%	0,14%	0,02553	0,04%	0,04%	420	10	499	12	517	9	510	9
Ju08b003	begin		0,05652	0,06%	0,14%	0,63603	0,85%	1,54%	0,08165	0,11%	0,14%	0,02510	0,04%	0,04%	473	11	500	12	506	9	501	8
Ju08b004	begin		0,05674	0,07%	0,14%	0,64005	0,86%	1,56%	0,08185	0,11%	0,14%	0,02507	0,04%	0,04%	481	12	502	12	507	9	500	8
Ju08b013	end		0,05737	0,07%	0,14%	0,64299	0,91%	1,59%	0,08135	0,11%	0,14%	0,02499	0,03%	0,04%	506	12	504	12	504	9	499	8
Ju08b014	end		0,05797	0,07%	0,14%	0,66486	0,95%	1,65%	0,08325	0,11%	0,15%	0,02562	0,04%	0,04%	529	13	518	13	515	9	511	9
Ju08b015	end		0,05482	0,07%	0,13%	0,62971	0,91%	1,57%	0,08337	0,11%	0,15%	0,02516	0,03%	0,04%	405	10	496	12	516	9	502	8
Ju08c002	begin		0,05705	0,06%	0,11%	0,64522	0,85%	1,45%	0,08209	0,11%	0,15%	0,02516	0,03%	0,04%	493	9	506	11	509	9	502	8
Ju08c003	begin		0,05590	0,06%	0,10%	0,63972	0,84%	1,43%	0,08303	0,11%	0,15%	0,02523	0,03%	0,04%	448	8	502	11	514	9	504	8
Ju08c004	begin		0,05766	0,07%	0,11%	0,65281	0,89%	1,48%	0,08217	0,11%	0,15%	0,02544	0,04%	0,04%	517	10	510	12	509	9	508	8
Ju08c013	end		0,05615	0,07%	0,11%	0,62536	0,88%	1,43%	0,08075	0,11%	0,15%	0,02484	0,03%	0,04%	458	9	493	11	501	9	496	8
Ju08c014	end		0,05742	0,07%	0,11%	0,65902	0,95%	1,53%	0,08325	0,11%	0,15%	0,02537	0,03%	0,04%	508	10	514	12	515	9	506	8
Ju08c015	end		0,05570	0,07%	0,11%	0,64087	0,93%	1,49%	0,08345	0,11%	0,15%	0,02541	0,04%	0,04%	440	9	503	12	517	9	507	8
No23a00	begin		0,05641	0,06%	0,07%	0,64883	0,85%	1,22%	0,08347	0,11%	0,14%	0,02531	0,00032	0,00037	469	6	508	10	517	9	505	7
No23a00	begin		0,05675	0,06%	0,07%	0,63471	0,85%	1,21%	0,08113	0,11%	0,14%	0,02501	0,00032	0,00037	482	6	499	10	503	9	499	7
No23a00	begin		0,05671	0,06%	0,07%	0,65188	0,87%	1,24%	0,08336	0,12%	0,15%	0,02557	0,00032	0,00037	480	6	510	10	516	9	510	7
No23a00	begin		0,0563	0,06%	0,07%	0,63964	0,86%	1,22%	0,08241	0,12%	0,15%	0,02515	0,00032	0,00037	464	6	502	10	510	9	502	7
No23a02	end		0,05692	0,06%	0,07%	0,65378	0,93%	1,29%	0,0833	0,12%	0,15%	0,02544	0,00032	0,00037	488	6	511	10	516	9	508	7
No23a02	end		0,057	0,06%	0,07%	0,65193	0,91%	1,27%	0,08295	0,12%	0,15%	0,02515	0,00032	0,00037	492	6	510	10	514	9	502	7
No23a02	end		0,05599	0,06%	0,07%	0,6331	0,89%	1,24%	0,082	0,12%	0,15%	0,02532	0,00032	0,00037	452	6	498	10	508	9	505	7
No23b00	begin		0,05627	0,06%	0,07%	0,63949	0,93%	1,03%	0,08245	0,12%	0,12%	0,02519	0,00032	0,00039	463	6	502	8	511	8	503	8
No23b00	begin		0,05716	0,06%	0,07%	0,64833	0,91%	1,02%	0,08229	0,12%	0,12%	0,0256	0,00033	0,0004	498	6	507	8	510	8	511	8
No23b00	begin		0,05618	0,06%	0,07%	0,64229	0,91%	1,02%	0,08294	0,12%	0,12%	0,02499	0,00032	0,00039	459	6	504	8	514	8	499	8
No23b00	begin		0,05676	0,06%	0,07%	0,64873	0,89%	1,01%	0,08291	0,12%	0,12%	0,02554	0,00032	0,00039	482	6	508	8	513	8	510	8
No23b02	end		0,05627	0,07%	0,08%	0,63878	0,95%	1,06%	0,08233	0,12%	0,13%	0,02532	0,00031	0,00038	463	6	502	8	510	8	505	8
No23b02	end		0,05664	0,06%	0,07%	0,64804	0,93%	1,04%	0,08297	0,12%	0,13%	0,02527	0,00031	0,00038	478	6	507	8	514	8	504	8

Tab.2

					Data for Wetherill plot[3]									Ages[3]										-Pb Concordant age	
Sample	Identifier	Mnz#	Spot locatio	Zoning	$^{207}Pb/^{206}Pb$	1s abs	$^{207}Pb/^{235}U$	1s abs	$^{206}Pb/^{238}U$	1s abs	Rho	$^{208}Pb/^{232}Th$	1s abs	$^{207}Pb/^{206}Pb$	1s abs	$^{207}Pb/^{235}U$	1s abs	$^{206}Pb/^{238}U$	1s abs	$^{208}Pb/^{232}Th$	1s abs	U-Pb disc	**U-Th disc[4]**		2s abs
ARG 19	No23a00	Mnz14	core	low-Y	0,05060	0,00060	0,37949	0,00711	0,05446	0,00096	0,9	0,01639	0,00024	223	3	327	6	342	6	329	5	-4,6	**3,9**		
	No23a00	Mnz14	core	int-Y	0,04850	0,00058	0,35984	0,00677	0,05384	0,00095	0,9	0,01651	0,00024	124	1	312	6	338	6	331	5	-8,3	**2,1**		
	No23a00	Mnz14	rim	high-Y	0,04718	0,00054	0,35209	0,00655	0,05419	0,00097	1,0	0,01672	0,00025	58	1	306	6	340	6	335	5	-11,1	**1,5**		
	No23a00	Mnz14	rim	high-Y	0,04719	0,00054	0,34671	0,00644	0,05337	0,00095	1,0	0,01602	0,00023	59	1	302	6	335	6	321	5	-10,9	**4,2**		
	No23a01	Mnz14	rim	high-Y	0,05304	0,00063	0,39997	0,00750	0,05482	0,00098	0,9	0,01616	0,00023	331	4	342	6	344	6	324	5	-0,7	**5,8**	**341**	**11**
	No23a01	Mnz14	core	low-Y	0,05362	0,00060	0,40053	0,00737	0,05427	0,00097	1,0	0,01596	0,00023	355	4	342	6	341	6	320	5	0,4	**6,1**	**344**	**10**
	No23a01	Mnz6	core	high-Y	0,04672	0,00052	0,34731	0,00641	0,05405	0,00097	1,0	0,01554	0,00022	35	0	303	6	339	6	312	4	-12,1	**8,2**		
	No23a01	Mnz3	core	low-Y	0,05366	0,00075	0,40986	0,00859	0,05523	0,00101	0,9	0,01578	0,00024	357	5	349	7	347	6	316	5	0,6	**8,7**	**348**	**12**
	No23a01	Mnz3	core	low-Y	0,05091	0,00074	0,38909	0,00823	0,05540	0,00102	0,9	0,01533	0,00023	237	3	334	7	348	6	308	5	-4,2	**11,5**		
	No23a01	Mnz8	core	low-Y	0,05012	0,00073	0,39204	0,00837	0,05684	0,00105	0,9	0,01555	0,00023	201	3	336	7	356	7	312	5	-6,1	**12,5**		
	No23a01	Mnz8	rim	high-Y	0,06046	0,00089	0,43421	0,00917	0,05209	0,00095	0,9	0,01580	0,00024	620	9	366	8	327	6	317	5	10,6	**3,2**		
ARG 29	No23b00	Mnz5	core	high-Y	0,04671	0,00064	0,33727	0,00559	0,05260	0,00080	0,9	0,01725	0,00028	34	0	295	5	~~330~~	~~5~~	~~346~~	~~6~~	-12,0	-4,6		
	No23b00	Mnz5	rim/core	low-Y	0,04793	0,00067	0,35617	0,00602	0,05387	0,00083	0,9	0,01637	0,00027	96	1	309	5	338	5	328	5	-9,3	3,0		
	No23b00	Mnz2	core	low-Y	0,04709	0,00054	0,36473	0,00547	0,05610	0,00085	1,0	0,01699	0,00027	54	1	316	5	~~352~~	~~5~~	341	5	-11,4	3,2		
	No23b00	Mnz2	core	high/int-Y	0,04631	0,00056	0,33850	0,00520	0,05301	0,00081	1,0	0,01643	0,00026	14	0	296	5	333	5	329	5	-12,5	1,1		
	No23b01	Mnz9	rim	high-Y	0,04648	0,00061	0,34793	0,00565	0,05427	0,00083	0,9	0,01645	0,00026	23	0	303	5	~~341~~	~~5~~	~~330~~	~~5~~	-12,4	3,2		
	No23b01	Mnz9	core	low-Y	0,18607	0,00259	1,52869	0,02448	0,05974	0,00093	1,0	0,01511	0,00025	2708	38	942	15	~~374~~	~~6~~	~~303~~	~~5~~	60,3	19,0		
	No23b01	Mnz11	core	low-Y	0,04845	0,00058	0,34997	0,00538	0,05234	0,00080	1,0	0,01663	0,00026	121	1	305	5	329	5	333	5	-7,9	**-1,4**		
	No23b01	Mnz11	core	low-Y	0,04926	0,00058	0,35799	0,00544	0,05268	0,00081	1,0	0,01646	0,00026	160	2	311	5	331	5	330	5	-6,5	**0,3**		
	No23b01	Mnz11	rim	high-Y	0,05338	0,00064	0,37450	0,00578	0,05085	0,00078	1,0	0,01626	0,00026	345	4	323	5	320	5	326	5	1,0	**-2,0**		
	No23b01	Mnz20	core	high-Y	0,04698	0,00072	0,33071	0,00590	0,05104	0,00080	0,9	0,01667	0,00027	48	1	290	5	321	5	334	5	-10,6	**-4,1**		
	No23b01	Mnz20	rim	low-Y	0,04901	0,00074	0,34441	0,00616	0,05121	0,00082	0,9	0,01630	0,00026	148	2	301	5	322	5	327	5	-7,1	**-1,5**		
	No23b01	Mnz24	core	high-Y	0,04687	0,00070	0,33064	0,00584	0,05121	0,00079	0,9	0,01655	0,00026	43	1	290	5	322	5	332	5	-11,0	**-3,1**		
	No23b01	Mnz24	core	low-Y	0,05828	0,00114	0,43250	0,00934	0,05354	0,00088	0,8	0,01482	0,00023	540	11	365	8	336	5	297	5	7,9	**11,6**		
ARG 48b	Ju08c006	Mnz58	Core	igh-Y/low	0,05115	0,00092	0,35022	0,00773	0,04967	0,00090	0,8	0,01556	0,00025	248	4	305	7	312	6	312	5	-2,5	0,1		
	Ju08c007	Mnz59	Core	High-Y	0,05339	0,00112	0,54547	0,01353	0,07418	0,00138	0,7	0,02130	0,00035	345	7	442	11	~~461~~	~~9~~	~~426~~	~~7~~	-4,4	7,7		
	Ju08c008	Mnz57	**Core**	**igh-Y/low**	**0,05361**	**0,00100**	**0,39211**	**0,00893**	**0,05303**	**0,00096**	**0,8**	**0,01636**	**0,00026**	**355**	**7**	**336**	**8**	**333**	**6**	**328**	**5**	**0,8**	**1,5**	**334**	**12**
	Ju08c009	Mnz56	Core	Medium-Y	0,05584	0,00106	0,39324	0,00900	0,05105	0,00093	0,8	0,01597	0,00026	446	8	337	8	321	6	320	5	4,7	0,2		
	Ju08c010	Mnz56	Core	Low-Y	0,05269	0,00115	0,37788	0,00964	0,05204	0,00098	0,7	0,01557	0,00026	315	7	325	8	327	6	312	5	-0,5	4,5	327	12
	Ju08c011	Mnz55	Rim	Medium-Y	0,05513	0,00129	0,37930	0,01018	0,04995	0,00094	0,7	0,01562	0,00026	417	10	327	9	314	6	313	5	3,8	0,3		
	Ju08c012	Mnz55	Core	Low-Y	0,04840	0,00093	0,33991	0,00792	0,05091	0,00093	0,8	0,01599	0,00026	119	2	297	7	320	6	321	5	-7,7	-0,2		
ARG21	Ju08a006	Mnz55	Core	High-Y	0,05031	0,00085	0,35590	0,00626	0,05132	0,00070	0,8	0,01602	0,00028	209	4	309	5	323	4	321	6	-4,4	**0,4**		
	Ju08a007	Mnz30	Core	High-Y	0,05196	0,00087	0,33730	0,00594	0,04713	0,00064	0,8	0,01430	0,00025	284	5	295	5	~~297~~	~~4~~	~~287~~	~~5~~	-0,6	**3,3**	297	8
	Ju08a008	Mnz26	Core	High-Y	0,05001	0,00083	0,34893	0,00612	0,05062	0,00069	0,8	0,01583	0,00028	195	3	304	5	318	4	317	6	-4,7	**0,3**		
	Ju08a009	Mnz7	Core	High-Y	0,04879	0,00081	0,34771	0,00610	0,05170	0,00071	0,8	0,01587	0,00028	138	2	303	5	325	4	318	6	-7,2	**2,1**		
	Ju08a010	Mnz7	Core	High-Y	0,04893	0,00082	0,34800	0,00614	0,05161	0,00071	0,8	0,01600	0,00028	144	2	303	5	324	4	321	6	-7,0	**1,1**		
	Ju08a011	Mnz16	Core	Medium-Y	0,05155	0,00087	0,36991	0,00661	0,05206	0,00072	0,8	0,01599	0,00028	266	4	320	6	327	5	321	6	-2,4	2,0		
	Ju08a012	Mnz16	Rim	High-Y	0,04985	0,00085	0,35610	0,00638	0,05184	0,00072	0,8	0,01591	0,00028	188	3	309	6	326	5	319	6	-5,3	**2,1**		
	Ju08a013	Mnz16	Rim	High-Y	0,04849	0,00081	0,33799	0,00598	0,05056	0,00070	0,8	0,01573	0,00028	123	2	296	5	318	4	315	6	-7,5	**0,8**		
	Ju08a014	Mnz16	Core	High-Y	0,05254	0,00092	0,36114	0,00672	0,04988	0,00070	0,8	0,01536	0,00027	309	5	313	6	~~314~~	~~4~~	~~308~~	~~5~~	-0,2	**1,8**	314	9
ARG27	Ju08b006	Mnz56	Core	High-Y	0,05027	0,00124	0,36285	0,00912	0,05220	0,00093	0,7	0,01609	0,00028	207	5	314	8	328	6	323	6	-4,4	1,6		
	Ju08b007	Mnz58	Core	Low-Y	0,05897	0,00139	0,42181	0,01010	0,05192	0,00090	0,7	0,01551	0,00026	566	13	357	9	326	6	311	5	8,7	4,7		
	Ju08b010	Mnz52	Rim-core	High-Y	0,05226	0,00123	0,37062	0,00886	0,05143	0,00089	0,7	0,01550	0,00026	297	7	320	8	323	6	311	5	-1,0	3,8	323	11
	Ju08b011	mnz52	Rim	Low-Y	0,08657	0,00204	0,62877	0,01503	0,05273	0,00092	0,7	0,01509	0,00025	1351	32	495	12	331	6	303	5	33,1	8,6		

3 Discordance calculated as (1-(206Pb/238U age/207Pb/235U age))*100

4 Discordance calculated as (1-(208Pb/232Th age/206Pb/238U age))*100

Tab.3